

# Three-dimensional vortex dynamics in superfluid <sup>4</sup>He: Homogeneous superfluid turbulence

K. W. Schwarz

*IBM Research Division, Thomas J. Watson Research Center, P.O. Box 218, Yorktown Heights, New York 10598*

(Received 17 December 1987)

The behavior of a tangle of quantized vortex lines subject to uniform superfluid and normal-fluid driving velocities is investigated. The dynamical equation of the quantized vortices in the local approximation is supplemented by the assumption that when two such singularities cross, they undergo a reconnection. The properties of the dynamical equation, when combined with the assumption of homogeneity, imply numerous scaling relations, which are in fact observed experimentally. The primitive dynamical rules are utilized to perform extensive numerical simulations of the vortex tangle, using not only periodic, but also smooth-wall and rough-wall boundary conditions. All lead to the same homogeneous vortex-tangle state, although the case of periodic boundary conditions requires an additional trick to eliminate artificial features. The quantitative results obtained from these simulations are found to be in excellent absolute agreement with a large variety of experiments, including recent studies of the vortex-tangle anisotropy.

## I. INTRODUCTION

It has long been appreciated<sup>1</sup> that many of the dynamical phenomena exhibited by superfluid <sup>4</sup>He involve the appearance and motion of quantized vortex lines, and that these singularities provide a mechanism through which the superfluid can couple dissipatively to its environment. More specifically, the notion that superfluid <sup>4</sup>He (also referred to as He II) behaves as a frictionless fluid containing vortex filaments in addition to a freely moving population of thermally excited elementary excitations (the normal fluid) was well advanced by the early 1960's. Detailed fluid-dynamical calculations based on this picture had yielded convincing quantitative agreement when applied to relatively simple vortex configurations such as the vortex array<sup>2</sup> in rotating He II or the propagating quantized vortex ring.<sup>3</sup>

More recently, considerable progress has been made in extending the fluid dynamical approach to the more complicated problems raised by the phenomenon of superfluid turbulence. We recall that at low velocities He II is observed to flow in the frictionless, presumably laminar manner consistent with the ideal-fluid description. Above some critical velocity, however, it enters a chaotic state having the nature of a dynamically self-sustaining random tangle of quantized vortex lines (Fig. 1). This description having been well established experimentally,<sup>4</sup> the issue is to understand why such a state of motion exists and to calculate its properties.

Although the extensive literature of the field is replete with imaginative speculations to the contrary, it seems reasonable to assume that the physics determining the onset and development of superfluid turbulence is the same as that which describes the vortex array and the propagating vortex ring. This indeed is the point of view adopted by Vinen<sup>5</sup> in his remarkable pioneering studies. Developing a deeper understanding of superfluid turbulence in terms of the fluid dynamical description, however, has required significant further developments,<sup>6,7</sup>

which owe much to the field of classical hydrodynamics. The most important features of this new methodology are careful analysis of the motion of quantized vortices, especially as regards the relative importance of self-induced, nonlocal, and frictional effects; utilization of dynamical scaling arguments; recognition of the fact that line-line reconnections are the essential mechanism which sustains the chaotic vortex-tangle state; and introduction of numerical simulation as the only method capable of extracting quantitative predictions from the highly nonlinear underlying vortex dynamics.

A previous paper<sup>8</sup> has dealt with the dynamics of three-dimensionally configured quantized vortex lines, and the reader is referred to this earlier paper for the background and justification of the brief review we shall now give. If the curve traced out by a vortex filament is specified in the parametric form  $\mathbf{s}=\mathbf{s}(\xi,t)$ , then the instantaneous velocity of a given point of the filament can be approximated by the equation<sup>9</sup>

$$\dot{\mathbf{s}} = \beta \mathbf{s}' \times \mathbf{s}'' + \mathbf{v}_s + \alpha \mathbf{s}' \times (\mathbf{v}_{ns} - \beta \mathbf{s}' \times \mathbf{s}'') - \alpha' \mathbf{s}' \times [\mathbf{s}' \times (\mathbf{v}_{ns} - \beta \mathbf{s}' \times \mathbf{s}'')], \tag{1}$$

where the primes denote instantaneous derivatives with respect to the arc length  $\xi$ ,  $\alpha$  and  $\alpha'$  are temperature-dependent parameters<sup>10</sup> which measure the frictional force exerted by the normal fluid on the vortex line,  $\mathbf{v}_{ns} = \mathbf{v}_n - \mathbf{v}_s$  is the difference between the average normal-fluid velocity and the applied superflow field, and

$$\beta = (\kappa/4\pi) \ln(c / |\mathbf{s}''| a_0), \tag{2}$$

where  $\kappa$  is the quantum of circulation,  $c$  a constant of order 1,  $|\mathbf{s}''|$  the average curvature of the filament, and  $a_0 \approx 1.3 \times 10^{-8}$  cm the effective core radius of the filament. Since  $|\mathbf{s}''|$  is just the inverse of the local radius of curvature  $R$ , it is convenient to interpret  $(|\mathbf{s}''|)^{-1}$  as the characteristic radius of curvature in the vortex tangle. This definition avoids overweighting straight sections of

vortex, for which  $R \rightarrow \infty$ . The first term on the right of Eq. (1) is the motion which the vortex induces on itself because it is curved. It causes every point on the vortex filament to move in the direction of the local binormal with a speed equal to  $\beta/R$ . As illustrated in Fig. 6 of Ref. 8, this gives rise to a very complicated thrashing

about in the case of a three-dimensionally curving vortex filament. The second term shows that the vortex is washed along with any superflow fields superimposed on that of the vortex itself. The third and fourth terms reflect the fact that the normal fluid streaming past the vortex core exerts a frictional force  $\mathbf{f}$  per unit length given by

$$\begin{aligned} \mathbf{f}/\kappa\rho_s = & -\alpha\mathbf{s}' \times [\mathbf{s}' \times (\mathbf{v}_{ns} - \beta\mathbf{s}' \times \mathbf{s}'')] \\ & -\alpha'\mathbf{s}' \times (\mathbf{v}_{ns} - \beta\mathbf{s}' \times \mathbf{s}'') \end{aligned} \quad (3)$$

on the fluid in the neighborhood of the core. The resultant motion of the vortex is such as to pass this force on to the superfluid as a reaction force. The term in  $\alpha'$  is usually assumed to represent a small correction and has not been included in previous calculations. Since its importance is an issue to be investigated here, it will be carried along in the equations. We will usually be interested in the situation where  $\alpha, \alpha'$  are small compared to 1, so that the frictional motion is basically a perturbation on the ideal-fluid behavior of the first two terms. It is to be noted, however, that while the first two terms conserve line length, the frictional motion not only causes the preferential decay of the more highly curved regions of vortex line, it also gives rise to a ballooning outward of sections of the vortex line which experience a strong enough normal-fluid tailwind (see Fig. 7 of Ref. 8).

Equation (1) neglects all dynamical effects arising from other vortices or from any boundaries that may be present. As shown in Ref. 8, this is expected to be a good approximation (i.e., to order 10%) provided the vortex-vortex or vortex-image spacing is greater than  $\Delta \approx 2R/\ln(cR/a_0)$ . When two vortices happen to approach each other more closely than this, a local instability occurs in which the velocity field of each vortex acts to deform the other such that the two vortices are driven together at a point with their vorticity vectors oppositely directed. What happens to a classical vortex in this limit is a matter of current research.<sup>11</sup> For a quantized vortex, where the approach of the two filaments can be followed all the way down to the angstrom level, it is supposed that the end result is a vortex-vortex reconnection, leading to an immediate separation of the two vortices to macroscopic distances. Thus Eq. (1) must be supplemented by the statement that the only important consequence of the nonlocal interaction is that whenever two vortices approach each other closely enough, they will rather suddenly undergo a reconnection of the approximate form shown in Fig. 2(a). Similarly, a vortex approaching a boundary closely enough is assumed to undergo a reconnection of the approximate form shown in Fig. 2(b). As will be discussed later, the details of when and how the vortices are reconnected or of how they behave immediately thereafter have no significant influence on the behavior of the vortex tangle, so that one can be satisfied with the simplified models of Fig. 2. We shall refer to the approximate description consisting of Eq. (1) and Fig. 2 (as well as some later refinements) as the *reconnecting vortex-tangle model*.

Referring to Fig. 1, the following qualitative picture of the self-sustaining vortex-tangle state can now be offered.

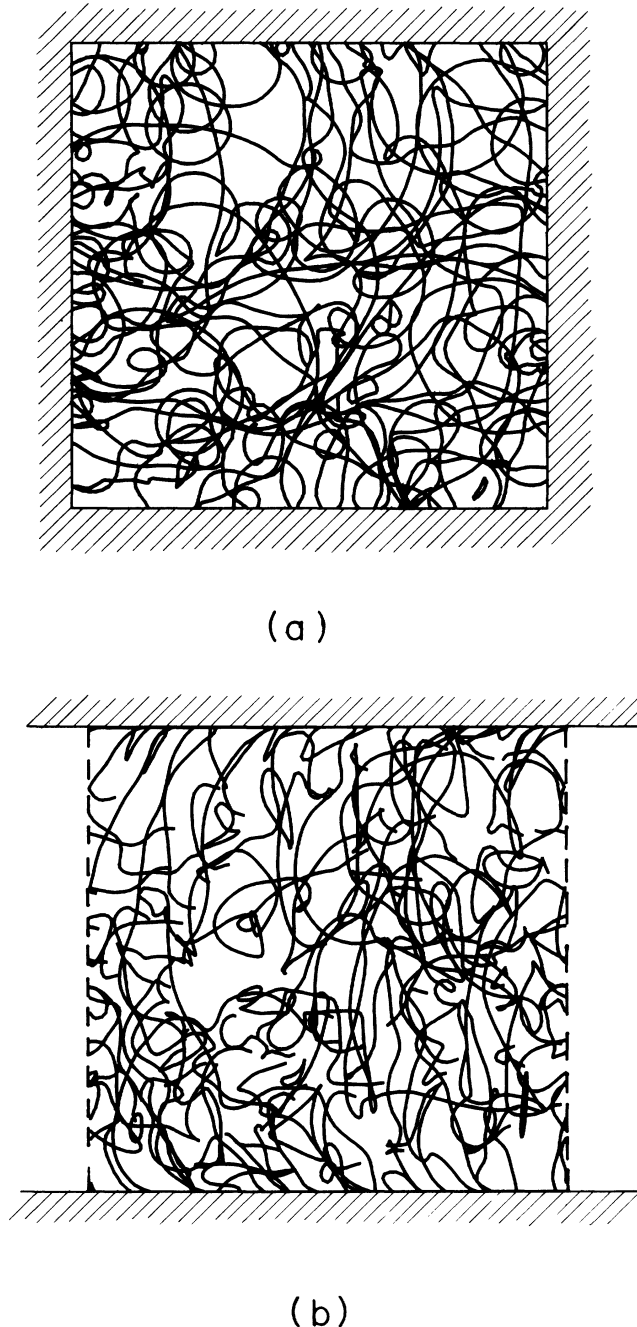


FIG. 1. Typical example of a vortex tangle in a rough channel, generated using the methods described in this paper. (a) A projection along the flow direction, and (b) a section of the channel viewed perpendicularly to the flow direction. The tangle is driven by a pure superfluid velocity field flowing from right to left (b). Note the atypical behavior very near the channel walls and the dragging of vortex lines by the surface roughness.

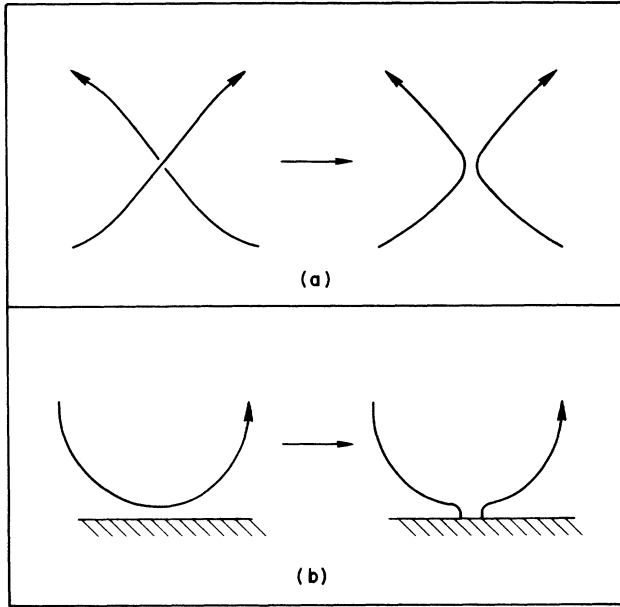


FIG. 2. Illustration of (a) a line-line reconnection, and (b) a line-surface reconnection. In actual calculations, the reconnections are made in a way very similar to this.

The self-induced velocity causes a complicated three-dimensional internal motion of the vortex tangle, the whole thing being washed along by any applied superflow field  $\mathbf{v}_s$ , which may be present. Highly curved sections of line, and sections propagating opposite to  $\mathbf{v}_{ns}$ , decay. Simultaneously, other parts of the vortex tangle where the self-induced motion is being overtaken by the  $\mathbf{v}_{ns}$  field grow by ballooning outwards. This cross-stream nature of the vortex growth implies that in the steady state at least a certain fraction of the singularities is constantly being driven toward the walls. The line-line reconnections which occur as the vortex tangle undergoes its complicated dance play several important roles. First, they provide a mechanism by which new vortex singularities can be created (Fig. 3), allowing the vortex tangle to be established and sustained against the loss of singularities at the walls. Secondly, and more subtly, since the vortex amplification process is essentially a two-dimensional outward motion in the plane perpendicular to  $\mathbf{v}_{ns}$ , the reconnections and the subsequent motions along  $\mathbf{v}_{ns}$  which results are necessary to maintain the three-dimensional random nature of the vortex tangle. Finally, reconnections occur more often as the tangle becomes denser. The increasing frictional line loss associated with the creation of a more and more highly curved vortex tangle is the factor which eventually limits the tangle density. All of these complicated dynamical features interact self-consistently to produce the turbulent steady state.

The above picture seems quite plausible. It is, however, far from obvious that Eq. (1) plus the reconnection mechanism lead to a self-sustaining vortex-tangle state, much less one which exhibits properties in agreement with experiment. That is precisely the issue which the present paper is intended to address. Consideration will

be restricted to the simple, limiting steady-state behavior observed experimentally when  $v_{ns}$  is kept constant and is much larger than the critical velocity for the onset of turbulence. The more complicated phenomena observed under other circumstances will be discussed in later papers.

It is the practice to characterize the intensity of superfluid turbulence by specifying  $L$ , the quantized-vortex line length per unit volume. Although some experiments have given information about the spatial and temporal variations of  $L$ , most measure  $\bar{L}$  averaged over time and over a fixed, experimentally probed volume. Many experiments involving superfluid turbulence under various conditions and using a variety of measuring techniques have been performed to determine  $\bar{L}$  in this gross fashion.<sup>4</sup> Essentially all find that if  $v_{ns}$  (the magnitude of  $\mathbf{v}_{ns}$ ) is large enough,  $\bar{L}$  obeys the relation

$$\bar{L}^{1/2} \approx \gamma(T, P)(v_{ns} - v_0), \quad (4)$$

where  $\gamma$  is a universal function depending only on the temperature and pressure,<sup>12</sup> and  $v_0$  is a small parameter of indeterminate origin. The fact that the measured average line-length density is independent of channel geometry has generally been interpreted to imply that the vortex tangle is in this limit spatially homogeneous, at least over most of the channel. In actuality, the vortex tangle interacts strongly with the channel walls and is usually driven at least partially by a normal-fluid-velocity field which must go to zero at the channel walls and hence be nonuniform across the channel. It is therefore not *a priori* obvious that the tangle should ever approach spatially homogeneous behavior. On the other hand, one can argue<sup>5</sup> that the effect of the walls on the vortex tangle

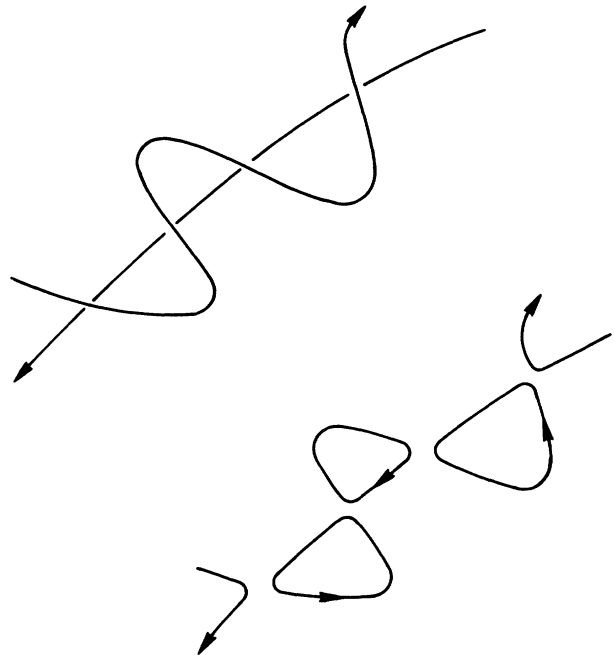


FIG. 3. Multiplication of singularities through the reconnection process. Here two vortex lines reconnect to form five.

should become negligible at higher line-length densities, when the characteristic line-line spacing  $\delta \simeq \bar{L}^{-1/2}$  becomes very small compared to the smallest cross-sectional dimension of the channel. It is moreover easy to see that the mutual friction forces acting between the vortices and the normal fluid are much greater than the viscous forces acting within the normal fluid. Except very near the walls, therefore, the normal-fluid-velocity profile should in fact be dominated by its interaction with the vortex tangle. These ideas are supported by a recent experiment<sup>13</sup> which employs pulsed-ion techniques to yield spatially resolved measurements of the line-length density and the normal-fluid velocity in a channel with a  $1 \times 2.3 \text{ cm}^2$  cross section. It is found that both  $\bar{L}$  and  $v_n$  are constant to a high degree of accuracy over almost the whole channel. This result implies that one is justified in interpreting channel experiments in terms of a homogeneous turbulence theory.<sup>14</sup> We note that the situation differs from that of classical turbulence, where it is well known that homogeneously turbulent channel flow is not possible, in that here the normal-fluid friction provides a driving mechanism which can act uniformly throughout the fluid.

Several distinct issues arise in exploring the implications of the reconnection model. The next section of this paper will be devoted to a discussion of how much one can conclude from this model if one simply *assumes* that the vortex tangle is spatially homogeneous. These general scaling considerations not only explain much of the functional behavior observed experimentally, but also provide a background for the more detailed considerations to come. Section III will describe the particulars of how the reconnection model has been implemented numerically to provide quantitative predictions. Finally, in Sec. IV, various computed properties of the homogeneous vortex-tangle state are reported and compared with selected experiments.

## II. DYNAMICAL SCALING

Dimensional analysis often yields nontrivial results when applied to nonlinear problems, and it is appropriate to consider what it can do here. Strictly speaking, no rigorous scaling is possible. It may be recalled from Ref. 8 that the ratio of the local to the nonlocal contributions is of order  $\ln(R/a_0)$ . Since the core size  $a_0$  is a fixed physical quantity, any attempt to multiply the vortex geometry (i.e.,  $R$ ) by some scaling factor will result in a change in the relative importance of the nonlocal corrections.

Within the context of the reconnection model, in which nonlocal corrections are neglected, this problem arises in vestigial form through the fact that the critical reconnection distance  $\Delta \simeq 2R / \ln(cR/a_0)$  does not scale linearly with  $R$ . However, the logarithmic variation is weak,  $\ln(cR/a_0)$  changing from about 18 at  $R = 1 \text{ cm}$  to about 7 at  $R = 10^{-5} \text{ cm}$ . If it can be shown that the properties of the vortex tangle are not very sensitive to the exact value of the reconnection distance, this distance can be treated as scaling along with the other dimensions. It will be demonstrated in Sec. III that such an assump-

tion is indeed justified (see Fig. 15). On this basis, the reconnection model leads to powerful *approximate* scaling arguments, capable of yielding unexpected predictions. Conversely, experimental verification of these predictions provides potent support for the validity of the model and for the existence of a homogeneous vortex-tangle state. The following is an elaboration of the ideas first presented in Ref. 7. A somewhat different elaboration has been offered by Swanson and Donnelly.<sup>15</sup>

The analysis of Eq. (1) is a simple two-step process. First, the factor  $\beta$  is absorbed into reduced time and velocity scales  $t_0 = \beta t$ ,  $v_0 = v / \beta$  to yield

$$\frac{\partial \mathbf{s}}{\partial t_0} = \mathbf{s}' \times \mathbf{s}'' + \mathbf{v}_{s,0} + \alpha \mathbf{s}' \times (\mathbf{v}_{ns,0} - \mathbf{s}' \times \mathbf{s}'') - \alpha' \mathbf{s}' \times [\mathbf{s}' \times (\mathbf{v}_{ns,0} - \mathbf{s}' \times \mathbf{s}'')] . \quad (5)$$

This equation is invariant under a transformation in which spatial dimensions are multiplied by a scale factor  $\lambda$ , times by  $\lambda^2$ , and velocities by  $\lambda^{-1}$ , subject to the previously mentioned *caveat* that the reconnection distances can also be assumed to scale with  $\lambda$  and that the critical angles are unchanged by the scaling.<sup>16</sup> If a vortex configuration contained in some particular geometry with dimensions  $D^*$  and subject to some particular set of velocities  $v_0^*$  has the particular evolution  $\mathbf{s} = \mathbf{s}^*(\xi^*, t_0^*)$ , one can then conclude that

$$\mathbf{s}(\xi, t_0) = \mathbf{s}(\lambda \xi^*, \lambda^2 t_0^*) = \lambda \mathbf{s}^*(\xi^*, t_0^*)$$

is the solution appropriate to  $D = \lambda D^*$  and  $v_0 = v_0^* / \lambda$ . Simply put, if all coordinates are magnified by the factor  $\lambda$ , and all applied velocities divided by the factor  $\lambda$ , then the vortex motion will still look the same, except that everything takes  $\lambda^2$  times as long to accomplish.

Suppose a specific value  $P^*(\mathbf{r}^*, t_0^*, v_0^*, D^*, \dots)$  of some property  $P(\mathbf{r}, t_0, v_0, D, \dots)$  of the vortices is calculated or measured in some particular geometry  $D^*$ . Interesting candidates for  $P$  might be the local line-length density, the density of the mutual friction force between the normal fluid and the vortex tangle, the characteristic radius of curvature of the vortex lines in the tangle, their structural anisotropy, or more esoteric things such as the reconnection rate, the fractal dimension of the tangle, or the power spectrum of fluctuations in  $L$ . These may, in general, depend not only on obvious variables of the type shown, but also on more subtle qualities such as the degree of surface roughness, the shape of the channel, the distance from the ends of the channel, or the length of time that the driving field has been applied. Because of the transformation properties of Eq. (5), one can then write

$$P(\mathbf{r}, t_0, v_0, D, \dots) = P(\lambda \mathbf{r}^*, \lambda^2 t_0^*, v_0^* / \lambda, \lambda D^*, \dots) = f(\lambda) P^*(\mathbf{r}^*, t_0^*, v_0^*, D^*, \dots) , \quad (6)$$

where  $f(\lambda)$  is obtained from the definition of  $P$ . Where such an equation applies, statements about the functional form of  $P$  are magically expanded into statements about how  $P$  scales with respect to various parameters. Conversely, information about how  $P$  scales leads to restrictions on its functional form.

Clearly,  $\lambda$  in Eq. (6) can be replaced by the appropriate ratio of final to initial values of whichever of the scaled quantities are deemed to be physically relevant. For example,  $\lambda$  might take the forms  $D/D^*$ ,  $v_0^*/v_0$ , or  $(t_0/t_0^*)^{1/2}$ , among others. Of course, these ratios are still in reduced units. To express  $\lambda$  and Eq. (6) in terms of the real world, one must make the identification  $t_0 = \beta t$ ,  $v_0 = v/\beta$ . Because  $\beta$  itself depends logarithmically on the scale through its dependence on  $|\mathbf{s}''|$ , this transformation will add logarithmic corrections to the scaling relations. While the logarithmic variation of  $\beta$  tends to become significant only when a wide range of channel sizes or driving velocities is involved, it is good practice when comparing experimental results with each other or with theoretical predictions to transform the data into universal form by expressing it in reduced units. Finally, it should be noted that the friction constants  $\alpha, \alpha'$  enter Eq. (5) as unscaled parameters: Because the equation is nonlinear, every set of values of these parameters in principle represents a separate problem. In discussing any property  $P$ , therefore, an unpredictable dependence on  $\alpha, \alpha'$  is understood.<sup>17</sup>

Equation (6) relates a particular situation to a set of others where the relevant variables take on a different collection of values. It is obviously useful in defining the amount of information necessary to completely characterize the property of interest. It will be recognized, however, that the greater the number of variables on which  $P$  depends, the less general and useful are the scaling relations which are obtained. Conversely, if Eq. (6) can be supplemented by the assertion that  $P$  is independent of all except a very few important parameters, rather powerful and surprising conclusions about the functional form of  $P$  can be drawn.

Suppose, for example, that the critical velocity for the onset of superfluid turbulence in a particular channel of cross-sectional dimension  $D^*$  is found to be  $v_{c,0}^* = v_c^*/\beta^*$ . Then since for velocities  $f(\lambda) = \lambda^{-1}$ , and expressing  $\lambda$  as  $D/D^*$ ,

$$v_{c,0} = (D^*/D)v_{c,0}^* . \quad (7)$$

This relation depends on the assumption that other variables such as channel length, cross-sectional shape, surface roughness, and so on either are scaled appropriately or do not affect the critical velocity. Thus the mere assertion that the critical velocity depends only on  $D$  leads immediately to the prediction (in real units and with  $\beta$  written out)

$$v_c = c_v \frac{\kappa}{4\pi D} \ln \left[ \frac{c'D}{a_0} \right] , \quad (8)$$

where  $c_v = D^* v_{c,0}^* = D^* v_c^*/\beta^*$ . Here it has been assumed that the characteristic radius of curvature at onset is some fraction of  $D$ , so that  $c'$  is some fraction of the constant  $c$  appearing in Eq. (2). This functional dependence of the critical velocity on channel size has long been established experimentally, and practically every critical velocity model, no matter how vague or farfetched, has managed to produce it, often with considerable fanfare. From our perspective, according to which the functional

form follows automatically from the equation for vortex motion, such an achievement is less than impressive. The constant  $c_v$ , on the other hand, cannot be calculated without a detailed understanding of what is happening at the onset—such questions constitute the real critical-velocity problem.<sup>18</sup>

Various ways of summing over the tangle need to be distinguished. Most basic is the line integral over all of the vortex line within some sample volume  $\Omega$ , evaluated for a particular instantaneous configuration of the tangle. This kind of sum will exhibit the intrinsic fluctuations associated with the tangle, the fluctuations taking on an increasing importance as the sample is made smaller. Such fluctuations are sometimes of interest. More usually, however, one will be interested in an ensemble-averaged property  $\bar{P}$ , by which we mean the integral averaged over all tangle configurations in accord with their probability of occurrence. In the steady state, the ensemble average will be the same as the time average. More generally,  $\bar{P}$  can represent a time-dependent quantity. For example, a study of transient behavior might involve averaging the transients generated from a suitably weighted collection of starting configurations to obtain an ensemble-averaged transient.

Consider now the line-length density

$$L = \frac{1}{\Omega} \int d\xi . \quad (9)$$

Suppose one measures a particular steady-state average  $\bar{L}^*$  at a point  $\mathbf{r}^*$  in a channel of characteristic width  $D^*$ , when the driving velocities are  $\mathbf{v}_{n,0}^*$  and  $\mathbf{v}_{s,0}^*$ . Although the argument can easily be given in terms of more complicated functional dependences on  $v_{n,0}$  and  $v_{s,0}$ , it will be assumed here than in fact  $\bar{L}$  depends only on the relative velocity  $v_{ns,0}$ . From Eq. (9) it is plain that for  $L$ ,  $f(\lambda) = \lambda^{-2}$ , so that

$$\begin{aligned} \bar{L}(\mathbf{r}, D, v_{ns,0}) &= \bar{L}(\lambda \mathbf{r}^*, \lambda D^*, v_{ns,0}^*/\lambda) \\ &= \lambda^{-2} \bar{L}^*(\mathbf{r}^*, D^*, v_{ns,0}^*) , \end{aligned} \quad (10)$$

where a number of the factors enumerated earlier have already been assumed to be irrelevant. If it is now asserted that  $\bar{L}$  does not depend on position within the channel or on channel size, and  $\lambda$  is expressed as  $v_{ns,0}^*/v_{ns,0}$ , it follows that

$$\bar{L} = c_L^2 v_{ns,0}^2 \quad (11)$$

or, in real units

$$\bar{L} = c_L^2 (v_{ns}/\beta)^2 , \quad (12)$$

where  $c_L^2 = \bar{L}^*/v_{ns,0}^{*2} = \bar{L}^* \beta^{*2}/v_{ns}^{*2}$ . Such a state, in which the time average of  $L$  is independent of position or any geometrical features, will be referred to as the *homogeneous* state. To put the above argument more concretely, for such a state one can take  $\bar{L}$  at a single velocity, and scale various channel sizes and positions back to a single channel size and position at various velocities, thus immediately obtaining Eq. (11).

It is not difficult to see that of the three requirements, namely spatial homogeneity, independence from  $D$ , and

$v_{ns,0}^2$  velocity dependence, any two imply the third. It must be noted here, however, that arguments of this type depend on the fact that the property in question is a well-defined, single-valued function of the relevant variables. In the case of  $\bar{L}$ , it is in fact quite possible to construct spatially homogeneous vortex states that will not change when the driving velocity is increased. The first of these is somewhat artificial, but will be of interest in discussing the vortex-tangle simulations. Consider a three-dimensionally periodic space filled with a uniform random distribution of straight vortex lines lying only in planes perpendicular to the driving velocity  $\mathbf{v}_{ns}$ . If it is assumed that the reconnection distance has some value less than the spacing between the lines, then the lines will always remain straight and never reconnect. Below a certain value, therefore,  $\bar{L}$  will not depend on the driving velocity and Eq. (11) does not apply. A second, less artificial example of interest is the case when a uniform distribution of vortices exists which are pinned by roughness on the channel walls. It can be shown that below some critical density, such vortices do not act on each other sufficiently strongly to reconnect.<sup>19</sup> Thus they reach a stationary state not uniquely related to  $v$ . In this case, as well, spatially homogeneous, steady-state behavior without  $v_0^2$  scaling arises because the vortex lines cannot interact dynamically through the reconnection mechanism.

For a numerical simulation of the vortex tangle, an inconsistency between the three conditions given above is a sign of serious trouble. It either indicates that the vortex tangle has degenerated into a collection of noninteracting lines, i.e., that there is no steady-state, dynamically active vortex tangle within the context of the simulation, or it implies a faulty calculation. Thus a demonstration of the simultaneous validity of all three conditions is an important test of any simulation purporting to describe the homogeneous limit.

Whether or not a homogeneous vortex tangle exists within the context of our model will be discussed in the next section. The discussion here, however, already provides grounds for optimism in view of the fact that all experiments, when carried out at sufficiently high velocities, have given the result of Eq. (12). Although previously Eq. (4) had been used to correlate the data, reexamination of some of the better experiments in view of our prediction has shown the remarkable accuracy with which Eq. (12) is obeyed. As will be discussed in Sec. IV, even the weak logarithmic dependence of  $\beta$  on  $|\mathbf{s}''|$  is clearly observed. This has been emphasized by Swanson and Donnelly.<sup>15</sup> Experts in the dynamics of classical fluids are often skeptical about the omission of nonlocal effects such as vortex-line stretching from any model purporting to describe a kind of turbulence. However, the experimental observation of precisely the predicted scaling behavior offers a solid indication that a homogeneous vortex-tangle state exists within the context of Eq. (1).

There is no difficulty in extending the scaling arguments to other quantities of interest. For the homogeneous state, to which the present discussion is restricted, it is sometimes convenient to use  $(\bar{L}^* / \bar{L})^{1/2}$  as the scaling parameter  $\lambda$ , as can readily be seen to follow from Eq.

(10). Thus, for example, the line-length weighted curvature  $(\Omega L)^{-1} \int |\mathbf{s}''| d\xi$  obeys

$$|\overline{\mathbf{s}''}| = c_1 \bar{L}^{1/2}, \quad (13)$$

where the explicit form of the constant will no longer be given since it is trivial to establish in each case. The characteristic radius of curvature  $|\overline{\mathbf{s}''}|^{-1}$  or any other characteristic distance in the tangle, such as, for example, the average interline spacing  $\delta$ , will therefore scale as  $\bar{L}^{-1/2}$ . Similarly,

$$|\overline{\mathbf{s}''}|^2 = c_2^2 \bar{L}, \quad (14)$$

a result which will prove useful later.

A plethora of other scaling relationships can be derived, of which we choose only those with particular relevance to the interpretation of past experimental work. An especially important set of properties relates to the fact that even though the vortex state may be homogeneous, it need not be isotropic: Because the vortices tend to grow by ballooning outwards in the plane perpendicular to  $\mathbf{v}_{ns}$ , the vortex lines can be expected to run preferentially in such planes, the quantity  $\mathbf{s}' \times \mathbf{s}''$  then being preferentially oriented parallel to the driving velocity. It is, of course, required that on average the distribution  $\mathbf{s}', \mathbf{s}'', \dots$  be rotationally symmetric about the preferred direction defined by  $\mathbf{v}_{ns}$ , and that the probability of  $\mathbf{s}'$  be the same as  $-\mathbf{s}'$ . Although the characterization of the anisotropy is to some extent a matter of choice, experiments define certain measures

$$I_{\parallel} = \frac{1}{\Omega L} \int [1 - (\mathbf{s}' \cdot \hat{\mathbf{r}}_{\parallel})^2] d\xi, \quad (15)$$

$$I_{\perp} = \frac{1}{\Omega L} \int [1 - (\mathbf{s}' \cdot \hat{\mathbf{r}}_{\perp})^2] d\xi, \quad (16)$$

$$I_I \hat{\mathbf{r}}_{\parallel} = \frac{1}{\Omega L^{3/2}} \int \mathbf{s}' \times \mathbf{s}'' d\xi \quad (17)$$

which need to be calculated if a comparison with theory is to be possible. Here  $\hat{\mathbf{r}}_{\parallel}$  and  $\hat{\mathbf{r}}_{\perp}$  stand for unit vectors parallel and perpendicular to the  $\hat{\mathbf{v}}_{ns}$  direction. As defined, the averages of these measures are independent of scaling, sample size, and line-length density for the homogeneous state. It is not difficult to show that if the tangle is isotropic,  $\bar{I}_{\parallel} = \bar{I}_{\perp} = \frac{2}{3}$ , and  $\bar{I}_I = 0$ . At the other extreme, if the tangle consists entirely of curves lying in planes normal to  $\mathbf{v}_{ns}$ , then  $\bar{I}_{\parallel} = 1$  and  $\bar{I}_{\perp} = \frac{1}{2}$ , with  $\bar{I}_I$  depending on the more subtle consideration of how the binormal is distributed. The relation

$$\bar{I}_{\parallel} / 2 + \bar{I}_{\perp} = 1 \quad (18)$$

which follows from the symmetry of the problem<sup>15</sup> will prove to be useful.

Several quantities of experimental relevance can be expressed in terms of the scale-invariant anisotropy coefficients defined above. Of greatest interest historically is the mutual friction force density  $F_{sn}$  exerted by the normal fluid on the superfluid. From Eq. (3) it follows that

$$\mathbf{F}_{sn} = -\frac{\rho_s \kappa \alpha}{\Omega} \int \mathbf{s}' \times [\mathbf{s}' \times (\mathbf{v}_{ns} - \beta \mathbf{s}' \times \mathbf{s}'')] d\xi, \quad (19)$$

the term in  $\alpha'$  vanishing by symmetry. Hence.

$$\bar{F}_{sn} = \rho_s \kappa \alpha (c_L^2 \bar{I}_{\parallel} - c_L^3 \bar{I}_l) v_{ns}^3 / \beta^2, \quad (20)$$

in the  $\hat{\mathbf{v}}_{ns}$  direction, where  $c_L$  is defined in Eq. (11). Similarly, the drift velocity of the vortex tangle with respect to the superfluid rest frame

$$\mathbf{v}_l = \frac{1}{\Omega L} \int \dot{\mathbf{s}} d\xi - \mathbf{v}_s, \quad (21)$$

where  $\dot{\mathbf{s}}$  is given by Eq. (1), averages to

$$\bar{\mathbf{v}}_l = [c_L(1 - \alpha') \bar{I}_l + \alpha' \bar{I}_{\parallel}] \bar{v}_{ns}, \quad (22)$$

in the direction of  $\hat{\mathbf{v}}_{ns}$ . Here the term in  $\alpha$  has vanished by symmetry. Again, Eqs. (20) and (22) have the form of scaling relations, which could just as well have been derived using Eq. (6) and the definitions. Thus the expression in parentheses in Eq. (20) is just the force coefficient  $F_0^*/v_0^{*3}$  defined in Ref. 7. Here, we have gone a step farther by expressing such coefficients in terms of the more fundamental parameters  $c_L$ ,  $\bar{I}_{\parallel}$ , and  $\bar{I}_l$ . By using Eq. (12), Eq. (20) can be rewritten in the useful alternative form

$$\bar{F}_{sn} = \rho_s \kappa \alpha (\bar{I}_{\parallel} - c_L \bar{I}_l) \bar{L} v_{ns}. \quad (23)$$

The above results provide a clarifying perspective on the way in which past experimental work should be used to test theoretical predictions. The vast majority of experiments done on the homogeneous vortex state determine  $\bar{F}_{sn}$  by exploiting the fact that it gives rise to a measurable temperature gradient  $\nabla T = \bar{F}_{sn} / \rho_s S$  along the flow direction, where  $S$  is the entropy per unit mass.  $\bar{L}$  is then deduced from Eq. (23) by assuming that the vortex tangle is isotropic, i.e.,  $\bar{I}_{\parallel} = \frac{2}{3}$  and  $\bar{I}_l = 0$ . Given the range of the anisotropy measures, this determination of  $\bar{L}$  is likely to be accurate to 10 or 20%. Independent confirmation at this level of accuracy has come from second-sound attenuation measurements<sup>5,20</sup> and ion-trapping experiments.<sup>13</sup> The relative accuracy is, of course, expected to be much better, so that, for example, the functional dependence of  $\bar{L}$  on  $v_{ns}$  can be tested quite precisely using this type of data analysis. In general, however, the accurate absolute interpretation of a given experiment requires anisotropy to be taken into account, as in the equations above. For the quantities that have so far proven to be of experimental interest, this is accomplished by calculating the parameters  $c_L$ ,  $\bar{I}_l$ , and either  $\bar{I}_{\parallel}$  or  $\bar{I}_{\perp}$ .

It is of interest at this stage not just to predict a particular quantity such as  $\bar{F}_{sn}$  from the theory, but to derive the parameters  $c_L$ ,  $\bar{I}_{\parallel}$ , and  $\bar{I}_l$  from the experimental data,  $\bar{I}_{\perp}$  then being given by Eq. (18). This has not proved practical in the past since, in addition to an accurate measurement of  $\bar{F}_{sn}$ , it requires independent absolute determinations of  $\bar{v}_l$  and  $\bar{L}$  to an accuracy well beyond any which has been attained. An interesting new approach, pioneered by Donnelly and co-workers,<sup>21</sup> is to make use of the fact that the vortex tangle is expected to

act anisotropically on such propagating probes as second-sound waves and ion currents. To first order, a second-sound wave represents a propagating wave in the relative velocity field  $\mathbf{u}_{ns} = \mathbf{u}_n - \mathbf{u}_s$ , the two fluids counteroscillating so as to keep the total density constant. In the presence of the vortex tangle, this field obeys the equation

$$\mathbf{u}_{ns} - C_2^2 \nabla(\nabla \cdot \mathbf{u}) + \frac{\rho}{\rho_s \rho_n} \mathbf{f}_{sn} = 0, \quad (24)$$

where from Eq. (3)

$$\mathbf{f}_{sn} = -\frac{\rho_s \kappa}{\Omega} \int [\alpha \mathbf{s}' \times (\mathbf{s}' \times \mathbf{u}_{ns}) + \alpha' \mathbf{s}' \times \mathbf{u}_{ns}] d\xi \quad (25)$$

is the force density acting between  $\mathbf{u}_n$  and  $\mathbf{u}_s$  because of the vortex tangle. Although the main effect of this term is to cause an attenuation of the second-sound wave, the fact that  $\mathbf{f}_{sn}$  is not in general along  $\mathbf{u}_{ns}$  gives rise to other complications. The solution is simple only when the propagation direction  $\hat{\mathbf{r}}$  is parallel or perpendicular to the symmetry axis  $\hat{\mathbf{v}}_{ns}$ . For parallel propagation, one obtains a longitudinal wave which decays with an attenuation coefficient

$$\alpha_{\parallel} = \frac{\rho \kappa \alpha}{2 \rho_n C_2} \bar{I}_{\parallel} \bar{L}. \quad (26)$$

A similar equation governs perpendicular propagation. Thus by determining the second-sound attenuation coefficients  $\alpha_{\parallel}$  and  $\alpha_{\perp}$ , and making use of Eq. (18),  $\bar{I}_{\parallel}$ ,  $\bar{I}_{\perp}$ , and  $c_L$  can be determined. In particular, the anisotropy ratio  $\bar{I}_{\perp} / \bar{I}_{\parallel}$  is measured relatively directly. Simultaneous measurement of  $\bar{F}_{sn}$  then allows one to determine  $\bar{I}_l$ . Such an experiment has recently been performed by Wang, Swanson, and Donnelly<sup>21</sup> and will be discussed in Sec. IV.

Other measures of the tangle anisotropy may eventually prove to be of importance. For example, the fraction of the linelength seen when viewing the vortex tangle along the particular direction  $\hat{\mathbf{r}}$  is just

$$J(\hat{\mathbf{r}}) = \frac{1}{\Omega L} \int [1 - (\mathbf{s}' \cdot \hat{\mathbf{r}})^2]^{1/2} d\xi. \quad (27)$$

Again, in an anisotropic tangle this quantity will depend on the direction of  $\hat{\mathbf{r}}$ , and one can define  $J_{\parallel}$  and  $J_{\perp}$ . Aside from the intuitive appeal of these measures, which tell us what we would see if we could look at the tangle from various directions, they may be of some use in interpreting ion-trapping experiments. At least in the high-field limit, ions pulled through the superfluid see the vortex lines simply as curves with an effective capture width, and the ion trapping rate is then just proportional to  $J(\hat{\mathbf{r}})$ .

To conclude this section, we consider the dynamical balance between vortex-line growth and decay processes at or near equilibrium. The instantaneous fractional rate of change of the line length at some particular point on a vortex is equal to  $\mathbf{s}' \cdot \partial \mathbf{s}' / \partial t$ . Consequently, a given element of length  $\Delta \xi$  obeys

$$\frac{1}{\Delta\xi} \frac{\partial\Delta\xi}{\partial t_0} = \alpha[\mathbf{v}_{ns,0} \cdot (\mathbf{s}' \times \mathbf{s}'') - |\mathbf{s}' \times \mathbf{s}''|^2] - \alpha' \mathbf{v}_{ns,0} \cdot \mathbf{s}'', \quad (28)$$

which leads to

$$\frac{\partial L}{\partial t_0} = \frac{\alpha}{\Omega} \mathbf{v}_{ns,0} \cdot \int \mathbf{s}' \times \mathbf{s}'' d\xi - \frac{\alpha}{\Omega} \int |\mathbf{s}''|^2 d\xi, \quad (29)$$

where the term in  $\alpha'$  has been dropped for reasons of symmetry. In the steady state, the ensemble average of this equation must be zero. In addition, the assumption of homogeneity allows use of Eqs. (11) and (17) to obtain the equation

$$\frac{\partial \bar{L}}{\partial t_0} = \alpha \bar{I}_1 v_{ns,0} \bar{L}^{3/2} - \alpha c_2^2 \bar{L}^2, \quad (30)$$

where  $c_2$  is defined by Eq. (14). Strictly speaking, this is valid only when  $\partial \bar{L} / \partial t_0 = 0$ . It is, however, to be expected that the scaling coefficients do not change much for small deviations from the steady state. A linear-response argument then implies that Eq. (30) also describes the ensemble-averaged time-dependent behavior of  $\bar{L}$  near equilibrium. Setting  $\partial \bar{L} / \partial t_0$  to zero and comparing with Eq. (11) also implies that  $c_L = \bar{I}_1 / c_2^2$ , reflecting the fact that in the final analysis the equilibrium density of the tangle is achieved by balancing the mean anisotropy of the self-induced velocity  $\mathbf{s}' \times \mathbf{s}''$  against its magnitude. Equation (30) can then be reexpressed in terms of just those scaling coefficients we have chosen to emphasize

$$\frac{\partial \bar{L}}{\partial t_0} = \alpha \bar{I}_1 (v_{ns,0} \bar{L}^{3/2} - c_L^{-1} \bar{L}^2). \quad (31)$$

Equations (30) and (31) are of the form first devised by Vinen<sup>5</sup> to describe the growth and decay of superfluid turbulence. The conventional Vinen coefficients are given in terms of the more fundamental coefficients defined here by  $\chi_1 = \bar{I}_1$  and  $\chi_2 = 2\pi\alpha\beta\bar{I}_1/\kappa c_1$ . Because a more fundamental theory has been lacking, the Vinen equation has provided the major phenomenological approach to the interpretation of experiments. It is deduced here from arguments which are very general and which trace back directly to the fundamental equation of vortex motion in the local approximation. At the same time, we now see that these arguments apply only to the average time-dependent behavior near the steady state. Neither the average behavior far from the steady state, nor the intrinsic fluctuations of  $L$  about the average steady-state value are necessarily described by this equation, although it has frequently been applied to such phenomena. In addition, it is known<sup>5,22</sup> that the free decay of the turbulence proceeds much more slowly than indicated by Eq. (30), and hence must involve some additional physics. For the time being, only the average steady-state behavior will be considered. Fluctuations and transients will be explored in a later paper.

### III. COMPUTATIONAL CONSIDERATIONS

To investigate the implications of the reconnecting vortex-tangle model, an arbitrary initial configuration of

vortex-tangle model, an arbitrary initial configuration of vortex lines, subject to a fixed driving velocity  $v_{ns,0}$  is allowed to evolve according to Eq. (5), and its fate is tracked. The algorithms used for stepping the vortex configuration forward in time are discussed in Ref. 8. Vortices are reconnected in the manner shown in Fig. 2 when they approach to within  $\Delta$  of each other, as discussed above and in Ref. 8. The motion of the resultant smoothed kinks is handled with sufficient accuracy by our computational scheme. Since the calculation must be performed in a finite sample of the fluid, it is necessary to specify how boundaries are treated. In our calculations, the sample is always a rectangular box with one set of faces perpendicular to the flow direction  $\hat{\mathbf{v}}_{ns,0}$ . This set of faces is subject to periodic boundary conditions, that is, any line leaving the box appears to reenter it from the opposite face. The aim of this procedure is to make the fluid appear infinite in the direction of flow. Depending on the situation, the box may be chosen to be stationary, or to be moving, e.g., with the superfluid velocity. The other boundaries are treated in one of three ways: as periodic, if the intent is to make the fluid appear infinite in all directions; as smooth, rigid boundaries, in which case vortex lines approaching a face will reconnect to the wall as shown in Fig. 2(b), the end then gliding freely along the wall; or as rough, rigid boundaries, in which case vortex lines terminating on the wall undergo a complicated pinning and depinning motion as they move along. The second and third approaches are meant to represent the vortex tangle in an ideally smooth and in a real channel, respectively. Although developed to investigate critical velocities,<sup>18</sup> they will turn out to provide an important check on the calculations done with periodic boundary conditions.

The computational box is usually taken to be of unit size in all three directions, although sometimes a smaller dimension is used in the streamwise direction to save computer time. It should go without saying that, because the calculation is done in reduced units and can be scaled out to arbitrary dimension, no particular real scale is implied by our choice of computational box size.

The outcome of a typical numerical experiment is shown in Figs. 4 and 5. Here an initial configuration of six vortex rings is allowed to evolve in a rough channel under the influence of a pure superflow driving field. It is clear that this particular situation evolves towards a self-sustaining chaotic steady state with well-defined average properties independent of the initial conditions. To give some idea of what is and is not possible with this kind of approach, it is worth noting that the particular simulation shown here required about 20 h of central-processing-unit (CPU) time on an IBM 3090 mainframe. Thus these simulations, each of which must run for long enough to overcome transients as well as to allow a suitable average over the intrinsic fluctuations exhibited by the vortex tangle, require significant computing resources. Since the running time scales roughly as the square of the line-length density, it is not practical to go far beyond the order of complication shown in Fig. 4.

The focus of the present paper is the high-density, presumably homogeneous limit. The most realistic way

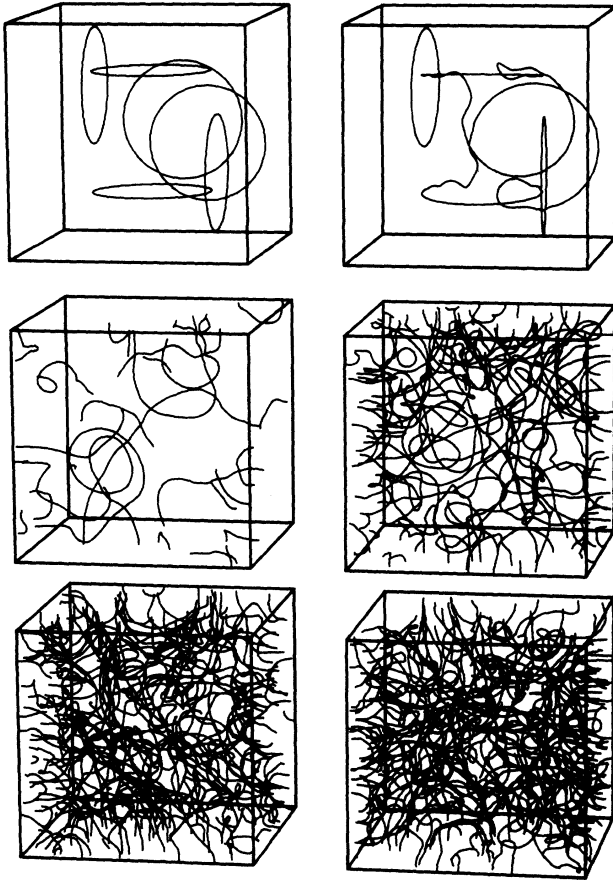


FIG. 4. Case study of the development of a vortex tangle in a real channel. Here,  $\alpha=0.10$ , corresponding to a temperature of about 1.6 K, and  $v_{s,0}=75$  into the front face of the channel section shown. Upper left:  $t_0=0$ , no reconnections; upper right:  $t_0=0.0028$ , three reconnections; middle left:  $t_0=0.05$ , 18 reconnections; middle right:  $t_0=0.20$ , 844 reconnections; lower left:  $t_0=0.55$ , 12 128 reconnections; lower right:  $t_0=2.75$ , 124 781 reconnections.

of trying to simulate this limit is to use rough-wall boundary conditions as in Fig. 4 and to sample the tangle near the center of the channel at driving velocities high enough to assure that  $\delta \ll D$ . This is a relatively expensive procedure because modeling the effects of surface roughness takes extra computation, because only a part of the tangle near the center of the channel can be used for taking averages, and because the driving velocity must be far above the critical velocity to approach homogeneous behavior. Smooth-wall boundary conditions are not much better. By far the most efficient method of generating the homogeneous limit is to use periodic boundary conditions on all faces. This kind of simulation effectively enforces spatially homogeneous behavior and is expected to be physically realistic provided the line density in the sample is high enough so that the vortices can maintain random behavior.

One objection to the use of periodic boundary conditions is that they introduce artificial features the implications of which bear investigation. It is now possible for a vortex leaving one side to reenter the opposite and con-

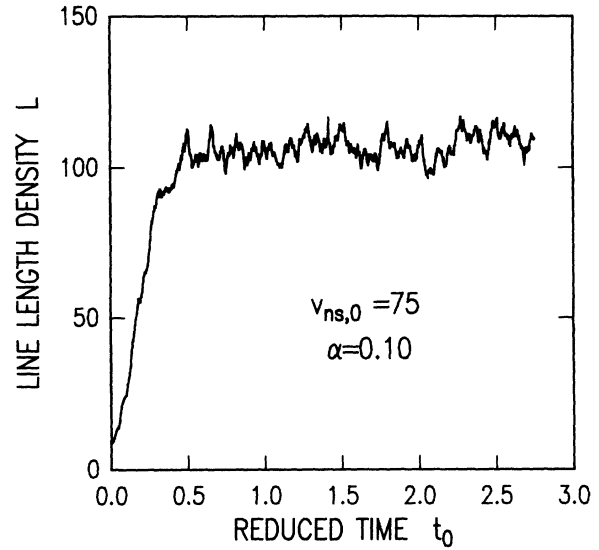


FIG. 5. Line length per unit volume as a function of reduced time for the run shown in Fig. 4. Note the occurrence of significant intrinsic fluctuations in  $L(t)$  after the tangle has reached the steady state.

nect to "itself," forming infinite vortex lines in the extended-zone representation. The simplest example of this is shown in Fig. 6. Because of the nonconservative vortex growth is across the flow direction, only reentry across the side faces is of concern. A given infinite line need not be periodic with the elementary box dimension but can map through the sample many times. Hence, it is not necessarily obvious when such lines are present. Unfolding any particular sample as in Fig. 7, however, shows that in practice even a very dense-looking sample consists primarily of a few infinite lines. This leads to an interesting qualitative insight about the nature of the vortex tangle. It has often been thought useful to visualize the vortex tangle as a gas of vortex rings with radii of order  $\delta$ . In actuality, the number of closed loops appears to be small, consisting mainly of small loops which have just been pinched off and which have not yet collided with another line. Larger vortex lines resemble the trail of a random walk and will either intersect a boundary (almost all of the lines in Fig. 4 terminate on the boundaries) or return to form a closed loop only after an enormous ex-

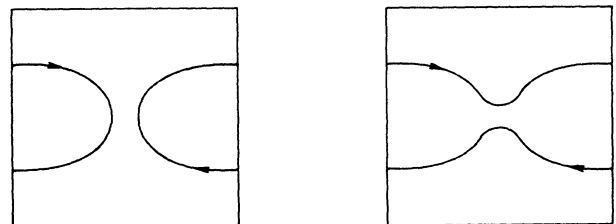


FIG. 6. A closed loop reconnecting to itself to produce two infinite lines. With  $v_{ns,0}$  into the figure, the closed loop would grow while the infinite lines will not.

cursion.

The dominance of infinite lines observed in the periodic boundary condition simulations presumably reflects the fact that these simulations have no hope of representing long-range features of the vortex tangle. Although it appears that this does not matter much in the determination of the tangle properties, the existence of infinite lines does lead to an interesting computational problem. We recall that the processes which sustain the vortex tangle involve a delicate balance between two- and three-dimensional effects. The line-amplification process takes place by the outward ballooning of vortex lines in the plane perpendicular to  $\mathbf{v}_{ns,0}$ , and if this were the only important mechanism, the tangle could not stay three-dimensionally random. In fact, the existence of the vortex tangle depends on a certain level of self-consistently maintained three-dimensional behavior in which vortex-vortex reconnections produce regions of high curvature, leading to three-dimensionally random self-induced motions, which in turn cause other reconnections. The



FIG. 7. Extended-zone view of a vortex tangle generated using periodic boundary conditions. Lines ending outside the computational volume are infinite. The vortex tangle fills all space with this configuration, with a periodicity determined by the sample cell dimensions.

periodic infinite lines created when periodic boundary conditions are imposed have a strong tendency to straighten out because of the preferential decay of the more highly curved sections. Once they begin to straighten out, they cease to grow and their self-induced velocity decreases. If they happen to approach a largely parallel configuration, so that they map into the computational unit cell as shown in the middle row of Fig. 8, the system will never be able to reestablish three-dimensional behavior. One may contrast this with the mapping of large loops, shown in the top row of Fig. 8, which, since it weighs all directions equally, favors random reconnections. We find that the replacement of large loops by periodic infinite lines disrupts the balance between two- and three-dimensional processes, preventing the maintenance of a dynamically active, homogeneous vortex-tangle state when periodic boundary conditions are imposed on the side faces. Although the details remain somewhat cloudy, it appears that sooner or later the simulation fluctuates into a dead-end state consisting

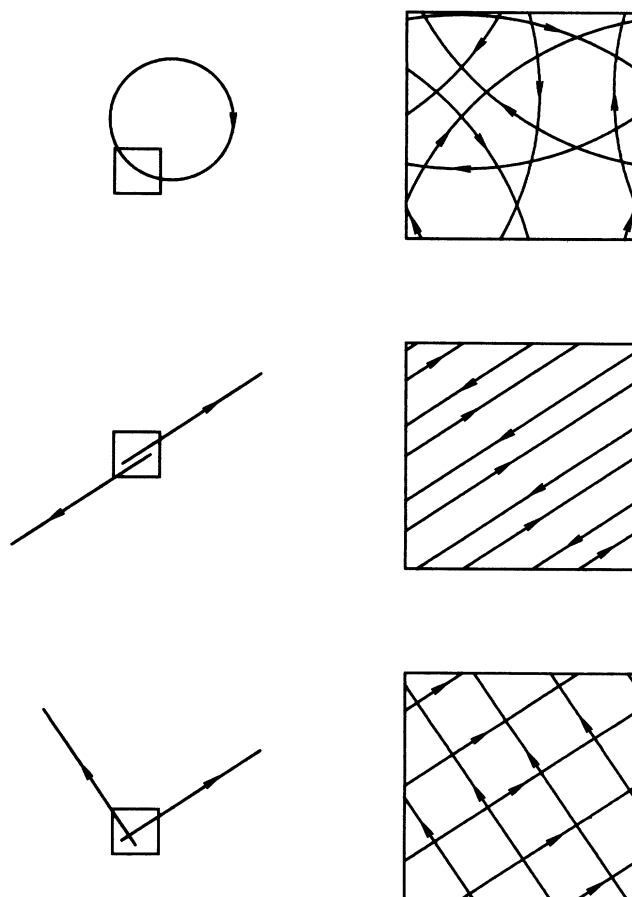


FIG. 8. Mapping of various vortex configurations into the computational volume, showing the appearance of the unit cell when all space is filled by the repetition of these objects. The end points of the lines represent equivalent points in the unit cell. Top row: closed loops; middle row: parallel infinite lines characteristic of a dead-end fluctuation; bottom row: infinite lines after randomizing procedure designed to reestablish three-dimensional behavior. The illustrations are intended to be purely schematic.

primarily of infinite lines which are sufficiently parallel so that three-dimensional behavior can never be re-established.

We have found that this presumably unphysical difficulty can be suppressed by the *ad hoc* procedure of adding an occasional mixing step to the simulation. In the mixing step, half of the infinite lines are randomly selected to be rotated by  $90^\circ$  around the axis defined by the flow velocity passing through the center of the box. For example, half of the lines terminating outside the box in Fig. 7 would be so rotated and then mapped back into the box. This procedure satisfies energy and momentum conservation and preserves the proper symmetry. Nevertheless, as is apparent from the bottom row of Fig. 8, it allows the simulation to escape from its occasional dead-end fluctuation. Provided the mixing step is applied sufficiently often, a dynamically stable, homogeneous vortex-tangle state is then achieved without difficulty. We have not investigated the required frequency of mixing at length, but find roughly that the time interval between mixing steps should be shorter than the characteristic time  $D/|s''|$  needed for an individual line to cross the computational volume. As  $\alpha$  becomes large, however, the mixing step needs to be applied more frequently to keep the vortex tangle three dimensional. Within these constraints, it is found that not only the average properties of the vortex tangle but also the relevant fluctuation spectra are, over a wide range, independent of the frequency with which the mixing step is applied (Fig. 9).

The somewhat artificial nature of the periodic boundary conditions, and the uncertain consequences of adding the heuristic mixing step, raise the possibility that such simulations distort the physics in some unrealistic way. Real-wall calculations, on the other hand, do not require

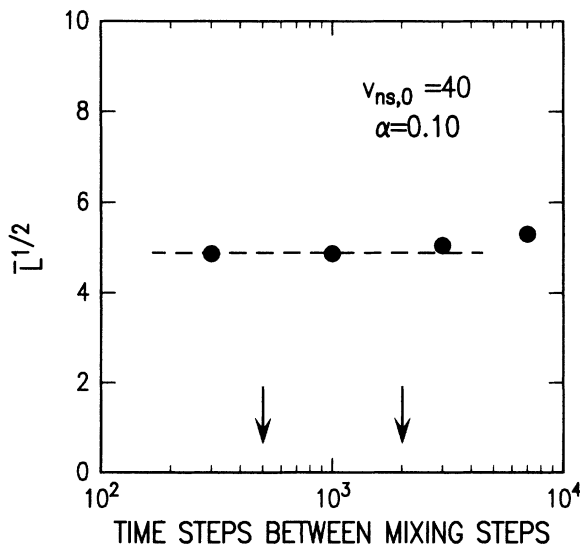


FIG. 9. Dependence of the calculated line-length density on the number of computational time steps between invocations of the mixing step. In this example,  $D/|s''|$  amounts to about 5000 time steps. Typical values used in computations lie between the two arrows.

the mixing procedure but they are expensive, and it is difficult to be certain that they fully attain the homogeneous limit. To resolve such doubts, an extensive intercomparison has been carried out between these quite different ways of generating the dense vortex-tangle state. This study was performed using  $\alpha=0.10$ ,  $\alpha'=0$ , and assuming (as always) a uniform driving velocity  $v_{ns,0}$ . The results are exhibited in Figs. 10 and 11. Each point shown is obtained from a study of the type illustrated in Fig. 5, covering a long enough reduced time interval to define accurate steady-state values. Figure 10 shows the average line-length density, evaluated in a  $(0.4)^3$  box centered in the  $(1.0)^3$  computational volume to avoid wall effects. It is observed, first, that while the results obtained using periodic boundary conditions with mixing lie systematically slightly lower, they are in good absolute agreement with those obtained using the two types of solid-wall conditions.<sup>23</sup> Secondly,  $\bar{L}$  as computed is found to be accurately proportional to  $v_{ns,0}^2$  as required by Eq. (11), implying that all of these methods produce results corresponding to the homogeneous limit. Figure 11 shows  $c_L$ , and various of the other important scaling coefficients derived from these runs. Again, all of the coefficients are substantially independent of  $\bar{L}$ , indicating that the simulations produce the homogeneous state and obey the scaling relations expressed by Eqs. (11), (13), (20), (23), and (31) to a high order of accuracy. The reader will again

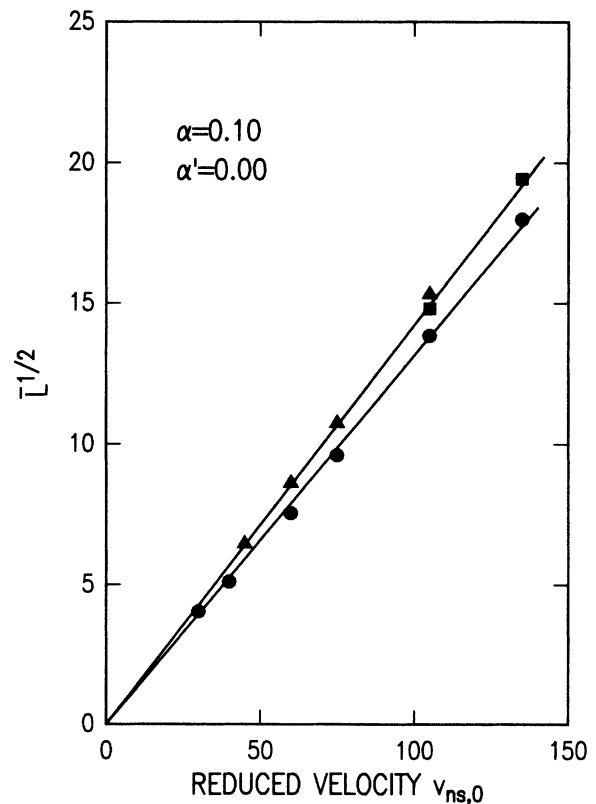


FIG. 10. Line-length density as a function of velocity calculated with rough walls (triangles), smooth walls (squares), and periodic boundary conditions with mixing (dots). The upper line is a fit to the real-wall calculations, the lower is a fit to the periodic boundary condition calculations.

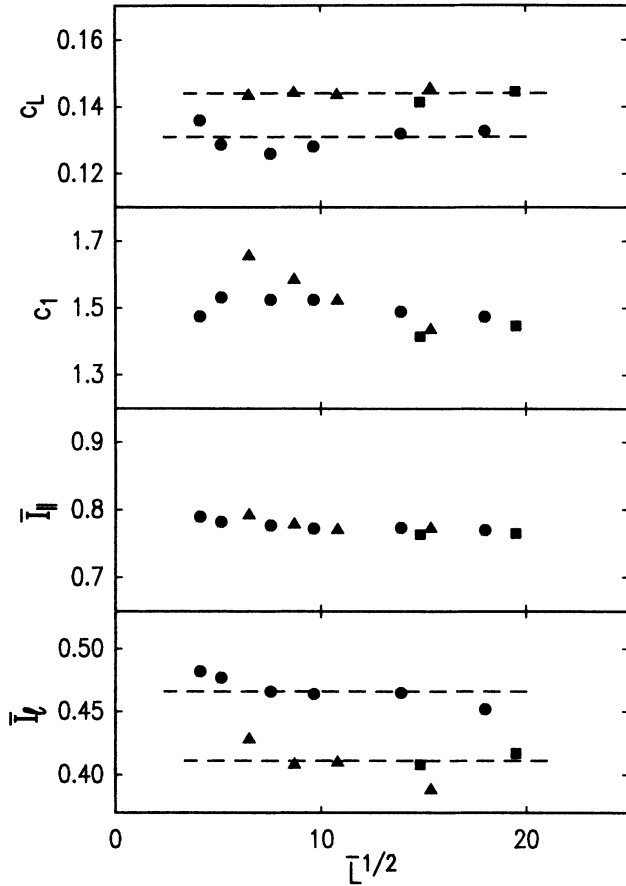


FIG. 11. Important scaling coefficients evaluated from the runs shown in Fig. 9. The lines have been drawn to guide the eye.

note the existence of some small systematic discrepancies between periodic and real-wall boundary conditions, but the overall agreement is very good.

The above results give one confidence that the use of periodic boundary conditions with a mixing step is a satisfactory way of reproducing the high-density limiting behavior of a system with real walls, and that this behavior is homogeneous. The remainder of the results reported in this paper were all obtained using periodic boundary conditions with mixing. On the basis of the results displayed in Figs. 10 and 11 (as well as other computational uncertainties to be discussed shortly), we estimate the absolute error in these results to be of order 10%. By happy coincidence, this is of the same magnitude as the errors involved in deriving Eq. (1) and is moreover typical of the accuracy with which the best experiments can be interpreted. Thus, agreement between experiment and theory to order 10 or 20% constitutes perfection here, and anything better is meaningless.

A host of other studies have been performed to validate our calculations. The following discussion provides a set of representative computations for  $v_{ns,0}=40$ ,  $\alpha=0.10$ , and  $\alpha'=0$  carried out within the context of periodic boundary conditions. A typical snapshot of the vortex tangle generated with these parameters is displayed in Fig. 12. Similar studies have also been car-

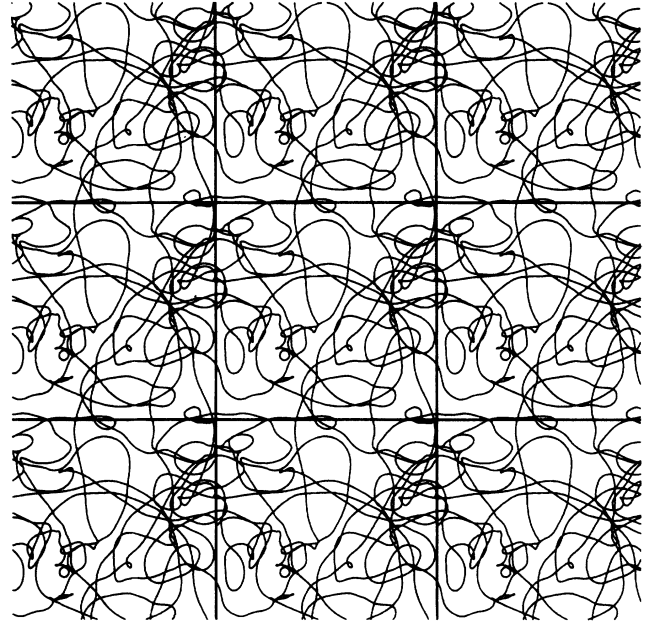


FIG. 12. A snapshot of the vortex tangle generated with  $v_{ns,0}=40$ ,  $\alpha=0.10$ , taken looking along the flow direction. The periodicity of the computational construct is illustrated explicitly.

ried out for real-wall boundary conditions. We first address the issue of numerical convergence. For a typical simulation, the spacing  $\delta\xi$  between points along the line is chosen to be an order of magnitude smaller than the characteristic radius of curvature  $|s''|^{-1}$ . Since  $|s''|$  scales linearly with  $v_{0,ns}$ , this means that  $\delta\xi$  must be scaled as  $v_{0,ns}^{-1}$ . The time step  $\delta t_0$  is then adjusted to be less than half the time step at which our algorithm shows signs of instability (see Ref. 8). Figure 13 illustrates that

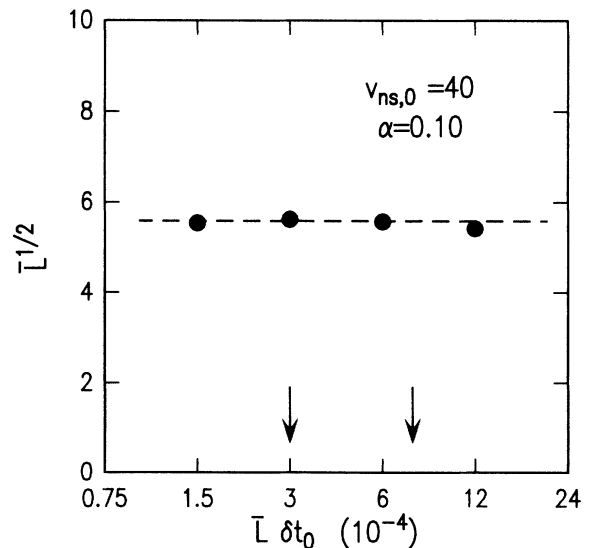


FIG. 13. Dependence of the calculated line-length density on time step. Here,  $\delta\xi=0.0125$  and  $\Delta=0.0125$ . The time step at which evidence of instability first occurs is  $\delta t_0 L \sim 15 \times 10^{-4}$ . Usual running conditions lie between the two arrows.

further reductions in the time step do not change the results. Figure 14 demonstrates that as expected on physical grounds the calculations are fully converged with respect to point spacing  $\delta\xi$  when  $\delta\xi |s''| \ll 1$ , and lose accuracy only gradually as  $\delta\xi$  is increased.

A separate issue to be considered is the extent to which the results depend on the choice of reconnection distance  $\Delta$ . In Ref. 8 we reported the results of fully nonlocal, infinitely-variable point spacing calculations of interacting vortex lines. There it was found that the reconnections are initiated when the lines are still a distance of order  $\Delta \simeq 2R / \ln(cR/a_0)$  apart, and that the end result of such an event is well approximated by making a smooth reconnection over a distance of order  $\Delta$  as shown in Fig. 2. As discussed in the previous section, the derivation of the various scaling relations depends on the assumption that the behavior of the vortex tangle is relatively insensitive to small variations in  $\Delta/R$ , i.e., to the variation of the logarithmic term in  $\Delta$  with the basic length scale  $L^{-1/2}$  in the vortex tangle. In Fig. 15 one sees how in fact the computed  $L$  varies with  $\Delta$ . The effect of varying  $\Delta$  is noticeable but, in view of the fact that  $L$  must vary by a factor of  $10^8$  in order to change the logarithm by a factor of 2, any effect on the scaling relations will be completely negligible.<sup>24</sup> The main effect of the  $\Delta$  dependence is that it introduces an uncertainty of order 10% in the determination of  $c_L$ , which is seen to depend to this extent on exactly how one chooses to make the reconnections.<sup>25</sup> As discussed earlier, this is comparable to other uncertainties in the calculations.

The  $\Delta$  dependence shown in Fig. 15 can be understood as arising from the fact that as  $\Delta$  becomes larger, the chance for reconnections increases. As the reconnection rate increases, more kinks are created, the characteristic

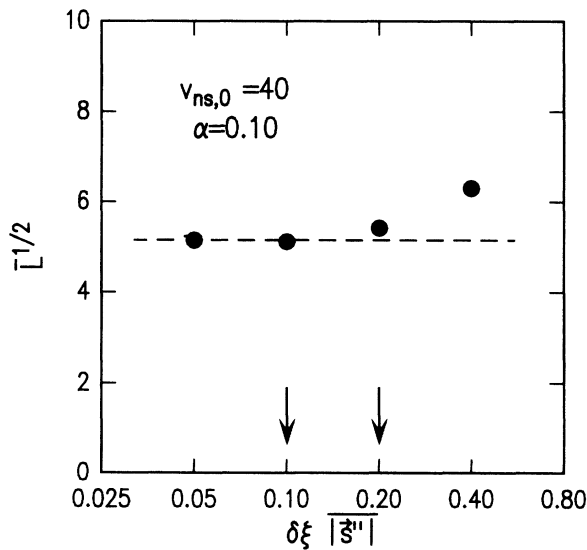


FIG. 14. Typical example of the change in the calculated values of  $\bar{L}$  as the spacing  $\delta\xi$  between the points used to describe the line is varied. For these calculations,  $\Delta=0.025$ . Usual running condition lies between the two arrows and is chosen to give good accuracy at minimum cost.

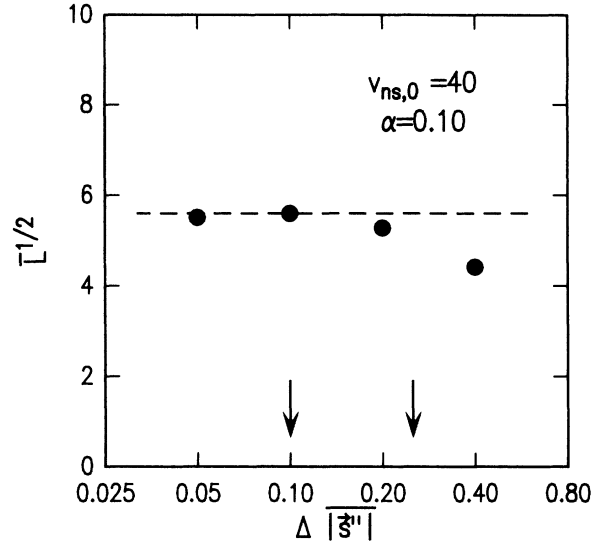


FIG. 15. Dependence of  $\bar{L}$  on reconnection distance  $\Delta$ . For these calculations,  $\delta\xi=0.0125$  and  $\delta t_0=2 \times 10^{-5}$ .

curvature and associated line loss [Eq. (29)] increases, and the tangle finds a new balance at a lower  $\bar{L}$ . The sensitivity of  $\bar{L}$  to the reconnection rate is dramatically illustrated in Fig. 16. Here, lines which pass within  $\Delta$  are reconnected only with some probability, rather than every time, as is the usual procedure. In accord with the above reasoning, a reduction in reconnection rates leads to a rapid increase in  $\bar{L}$ . It is furthermore of interest to point out that the agreement between theory and experiment to be discussed in the next section indicates that lines which encounter each other closely will in fact reconnect essen-

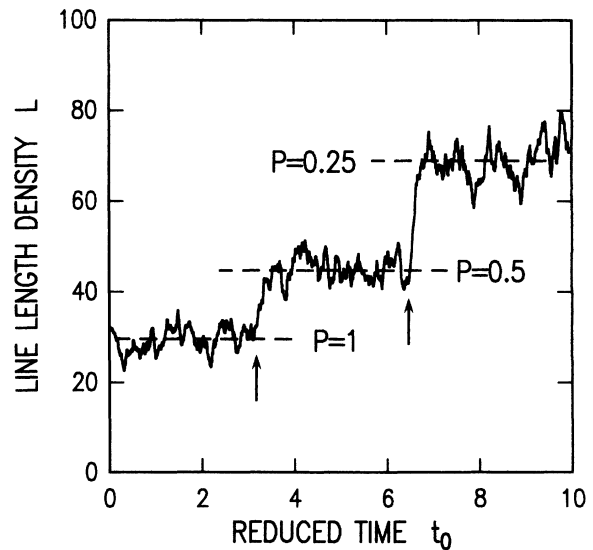


FIG. 16. Dependence of line-length density on reconnection probability. Here,  $v_{sn,0}=40$ ,  $\alpha=0.10$ ,  $\alpha'=0$ ,  $\delta\xi=0.0125$ ,  $\delta t_0=2 \times 10^{-5}$ ,  $\Delta=0.025$ . The arrows indicate the time during the run at which the probabilities were changed. The lines have been drawn to guide the eye.

tially every time. While this is implied by the fluid dynamical calculations of Ref. 8, it has still been to some extent an assumption of the theory, since the ultimate microscopic reconnection process is beyond the scope of the classical approximations.

We next address the question of whether the simulation using periodic boundary conditions with mixing produces turbulence which is homogeneous in the sense of Sec. II. It has already been demonstrated (Fig. 10) that  $\bar{L}$  is strictly proportional to  $v_{ns,0}^2$ . To demonstrate spatial uniformity, the average line length was evaluated in sampling volumes constructed by dividing the  $(1.0)^3$  computational volume into the concentric shells formed by the cubes  $(0.2)^3$ ,  $(0.4)^3$ ,  $(0.6)^3$ ,  $(0.8)^3$ , and  $(1.0)^3$ , and computing  $\bar{L}$  separately within each volume. Figure 17 shows that  $\bar{L}$  is the same in each shell to essentially perfect accuracy. This is to be contrasted with the results obtained when real-wall boundary conditions are specified (Fig. 18): Because of surface effects, there is now a boundary layer near the wall where  $\bar{L}$  varies significantly. Again, this effect would introduce errors of at most 10%. For the final test, the average value of  $L$  at a fixed driving velocity was computed using computational boxes of size  $(0.67)^3$ ,  $(1.0)^3$ ,  $(1.5)^3$ , and  $(2.0)^3$ , covering a range of about 25 in computational volume (Fig. 19). As expected, the results are independent of  $D$ , which in this case takes the meaning of the size of the computational box. The simultaneous validity of the three homogeneity conditions identified in Sec. II is therefore demonstrated. There is no reason to doubt that our implementation of the recon-

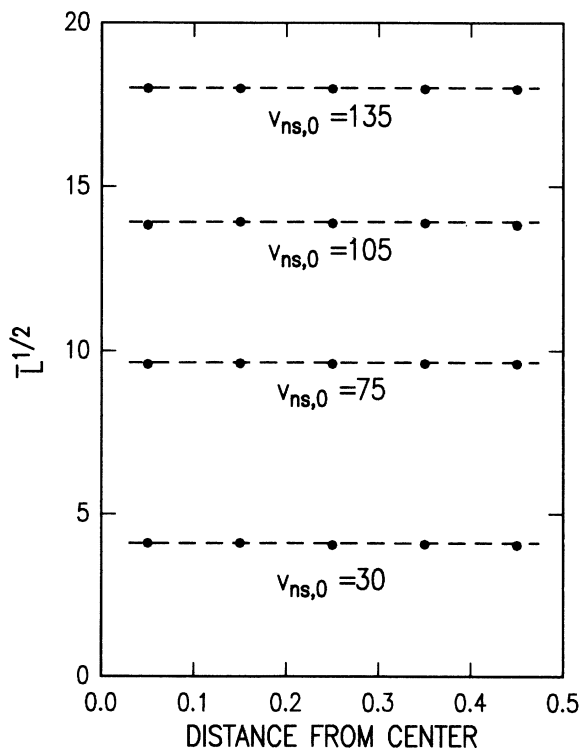


FIG. 17. Line-length densities evaluated in concentric shells of the computational volume for various driving velocities and  $\alpha=0.10$ . Periodic boundary conditions.

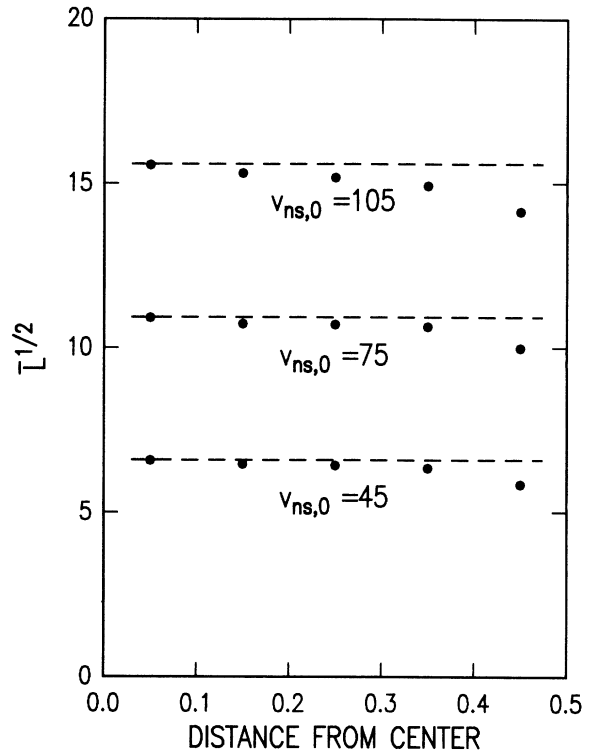


FIG. 18. Line-length densities evaluated in concentric shells of the computational volume for various driving velocities and  $\alpha=0.10$ . Rough-wall boundary conditions.

necting vortex-tangle model leads to a truly homogeneous state.

To complete this section, Fig. 20 shows the effects on a typical simulation of using nonzero values of  $\alpha'$ . Experimentally,  $\alpha$  and  $\alpha'$  cannot be varied independently, and since  $\alpha'$  becomes comparable to  $\alpha$  at lower temperatures,

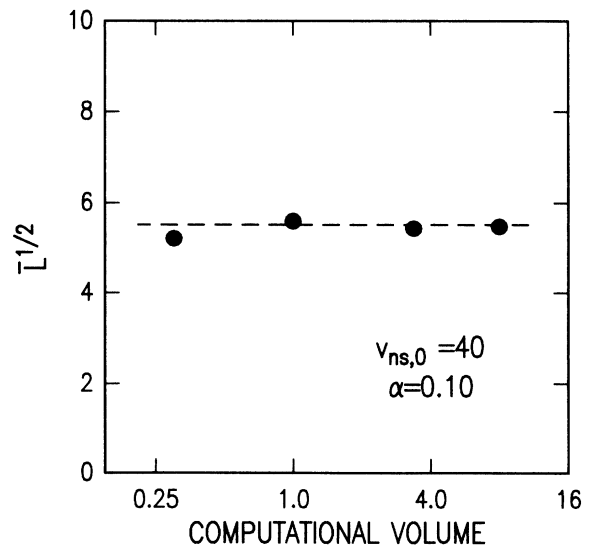


FIG. 19. Dependence of  $\bar{L}$  on computational volume. For these calculations,  $\delta\xi=0.0125$  and  $\Delta=0.0125$ . The tangle cannot be sustained below a computational volume of 0.25.

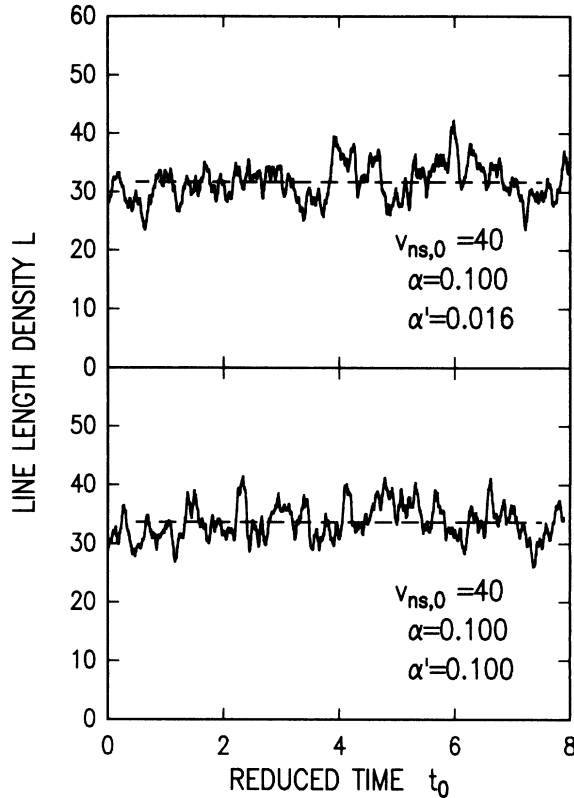


FIG. 20. Two runs illustrating the insensitivity of the vortex tangle to  $\alpha'$ . The dashed lines indicate average values derived from these samples. The difference is within the uncertainty arising from the intrinsic fluctuations and much less than other estimated errors discussed previously.

one might expect  $\alpha'$  to give rise to nonnegligible corrections. Somewhat unexpectedly, we find that even values of  $\alpha'$  comparable to  $\alpha$  lead to no significant changes in the behavior of the fully developed vortex tangle. This is probably ascribable to the fact that the  $\alpha'$  term in Eq. (28) averages to zero. While all of the results presented in the next section have in fact been calculated utilizing the appropriate nonzero values of  $\alpha'$ , the results are insensitive to this choice—it appears to be an excellent approximation to set  $\alpha'$  equal to zero in developing the theory.

#### IV. RESULTS

The theory presented in the previous sections makes specific, absolute predictions involving no adjustable parameters whatsoever. As discussed in Sec. III, these predictions are expected to be accurate at best to order 10% for quantities which vary linearly with  $v_{ns,0}$ , with correspondingly larger percentage errors for quantities which vary as a higher power. In the present section, the results of our theory are presented and compared with selected experimental measurements. The comparison is not intended to be exhaustive, but rather aims to illustrate the point that the theory provides a quantitative explanation for a variety of observations.

The various kinds of scaling predicted by the theory have been discussed in Sec. II. The actual values of the relevant scaling coefficients can be determined by measuring the properties of the simulated vortex tangle, generated as described in Sec. III. The results of these calculations, all of which were carried out using periodic boundary conditions with mixing as previously discussed, are given in Table I. For each  $\alpha$ , at least two runs were car-

TABLE I. Summary of numerical results. For each friction constant  $\alpha$  (and the associated  $\alpha'$  and  $T$ ) simulations at two velocities  $v_{ns,0}$  were carried out. The associated measured values of  $\bar{L}$  and of the scaling coefficients, as obtained from each individual run, are shown. The reproducibility of the scaling coefficients indicates both that reliable average values have been obtained and that homogeneous scaling holds to a high degree of accuracy.

$\alpha$	0.010	0.030	0.100	0.300	1.00
$\alpha'$	0.005	0.0125	0.016	0.010	-0.270
$T$	1.07	1.26	1.62	2.01	2.15
$v_{ns,0}$	140	55	40	20	25
$\bar{L}$	190	80	135	30	35
	24.5	16.0	31.7	19.4	45.8
	48.1	34.0	323.4	43.6	95.8
$c_L$	0.0353	0.0728	0.141	0.220	0.280
	0.0365	0.0729	0.133	0.220	0.280
$c_1$	2.91	2.00	1.41	1.02	0.718
	2.81	1.97	1.48	1.05	0.719
$c_2$	3.47	2.46	1.79	1.40	1.16
	3.33	2.42	1.84	1.43	1.14
$\bar{I}_{\parallel}$	0.721	0.746	0.787	0.875	0.954
	0.719	0.749	0.770	0.870	0.952
$\bar{I}_l$	0.437	0.454	0.461	0.440	0.355
	0.428	0.442	0.454	0.460	0.358
$\bar{J}_{\parallel}$	0.825	0.841	0.870	0.927	0.975
	0.823	0.844	0.858	0.924	0.973
$\bar{J}_l$	0.756	0.756	0.739	0.700	0.665
	0.766	0.755	0.745	0.705	0.667

ried out, with velocities sufficiently different to provide a variation in  $\bar{L}$  of at least a factor of 2. This not only permits a check on the validity of homogeneous scaling for each set of friction coefficients, but also provides a feel for the numerical accuracy with which the scaling coefficients can be evaluated from the fluctuating tangle. Although the reader can gather from Figs. 5, 16, and 20 that the fluctuations are in fact rather pronounced, the results of Table I illustrate that the individual runs (which typically have a duration  $\Delta t_0=8$ ) produce extremely well-defined average behavior. The variations of 1 or 2% seen here are negligible compared to other errors discussed previously. Various reductions of the data in Table I, useful for interpolation and required for the subsequent discussion, are given in Figs. 21–23. The temperature scales indicated in Table I and in the figures are based on Table I of Ref. 8. For convenience, the assumed relation between  $\alpha$  and  $T$  is reproduced in Fig. 24. It should be emphasized that this relation is approximate and that it may depend somewhat on the experimental circumstances.<sup>17</sup> For our purposes, Fig. 24 represents a reasonable compromise which introduces errors no greater than those already discussed.

The calculations have been carried out for  $\alpha$  as large as 1.0, but the theory may be expected to become less accurate in this limit. Among other reasons, the friction is no longer a small perturbation on the motion, the dragging of the normal fluid by the vortex becomes severe, and nonlocal velocity corrections may take on increased significance.

A most striking and direct illustration of the degree to which our theory matches experimental observation is shown in Fig. 25. The data points are obtained from Fig. 1 of the classic paper by Brewer and Edwards,<sup>26</sup> which

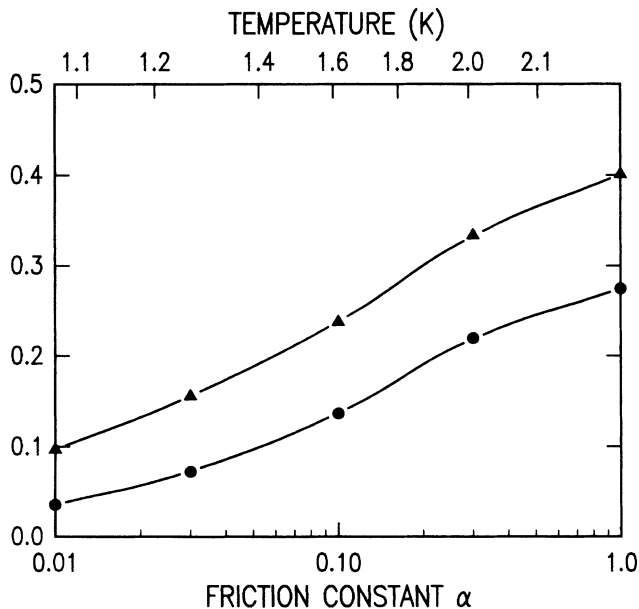


FIG. 21. Line-length density scaling coefficient  $c_L$  (dots) and mutual friction coefficient  $(c_L^2 \bar{I}_{\parallel} - c_L^2 \bar{I}_{\perp})^{1/3}$  (triangles) derived from Table I. The lines are cubic spline fits.

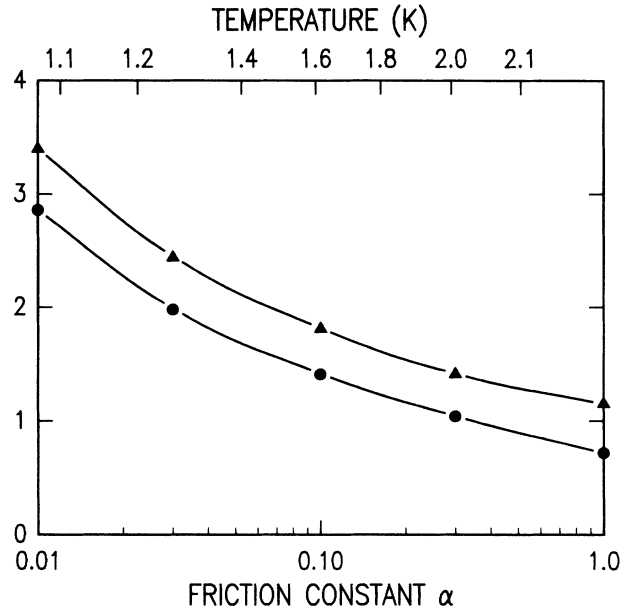


FIG. 22. Scaling coefficients  $c_1$  (dots) and  $c_2$  (triangles) as derived from Table I. The lines are cubic spline fits.

shows  $\bar{L}^{1/2}$  versus  $v_{ns}$  for various temperatures, as measured in a glass capillary tube with an internal diameter of 0.0366 cm. Since these authors deduce  $\bar{L}$  from their measurements of  $\bar{F}_{sn}$  by using the not-quite-correct formula

$$\bar{F}_{sn} = \frac{1}{3} B \frac{\rho_s \rho_n}{\rho} \kappa v_{ns} \bar{L}, \quad (32)$$

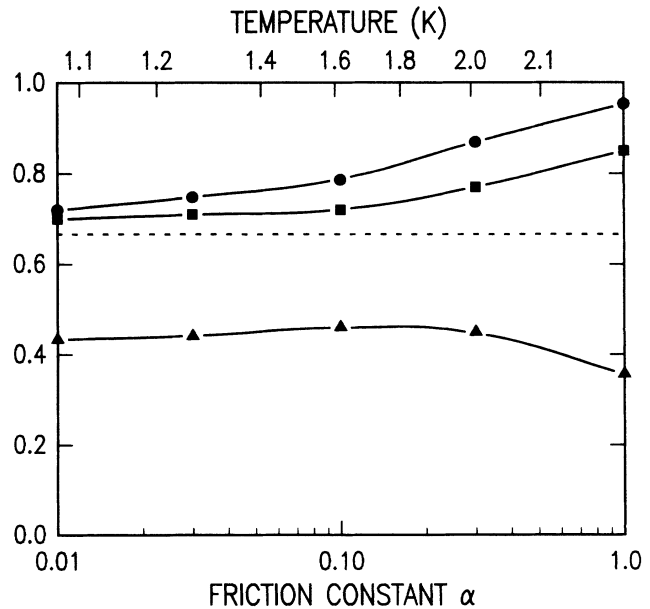


FIG. 23. Anisotropy coefficients  $\bar{I}_{\parallel}$  (dots) and  $\bar{I}_{\perp}$  (triangles) from Table I. The squares show the quantity  $\bar{I}_{\parallel} - c_L \bar{I}_{\perp}$ , which would equal  $\frac{2}{3}$  (dashed line) if the tangle were isotropic. The solid lines are cubic spline fits.

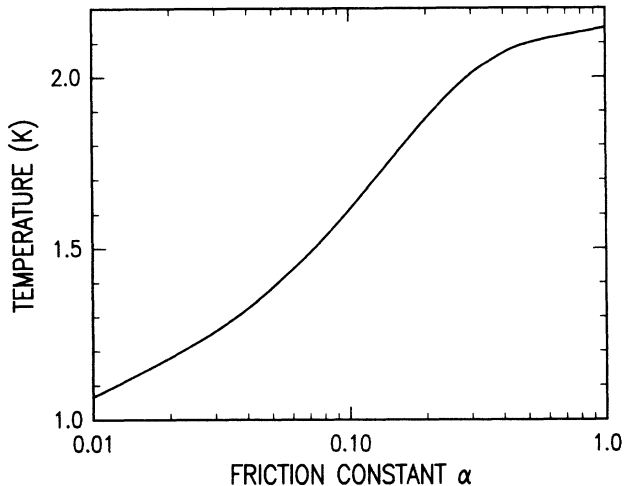


FIG. 24. Assumed relation between the friction constant  $\alpha$  and the temperature.

we have reconstituted their values of  $\bar{F}_{sn}$  using the original values<sup>2</sup> of  $B$ . The solid lines in Fig. 25, however, represent the prediction of Eq. (20). Here  $\alpha$  is obtained from Fig. 24,  $(c_L^2 \bar{I}_{\parallel} - c_L^3 \bar{I}_I)^{1/3}$  from Fig. 21, and  $\beta$  is taken to equal  $\kappa/4\pi \ln(1/c_1 \bar{L}^{1/2} a_0)$ , where  $c_1$  is obtained from Fig. 22, and  $\bar{L}$  is obtained self-consistently using Eq. (12) and  $c_L$  as read off Fig. 21. It is indeed remarkable that a calculation based simply on Eq. (1) and the reconnection concept, along with some practical input such as the dependence of  $\alpha$  on temperature, should be so successful in explaining a very complicated set of measurements made some 25 years ago.

A second example of the success of the theory is displayed in Fig. 26, which represents a very precise study by Martin and Tough<sup>27</sup> of the functional relationship between  $\bar{L}$  and  $v_{ns}$ . The upper half of the figure shows the historically accepted way of plotting such data. A straight-line fit results in a mysterious nonzero intercept [viz. Eq. (4)], as well as a slight upwardly curving de-

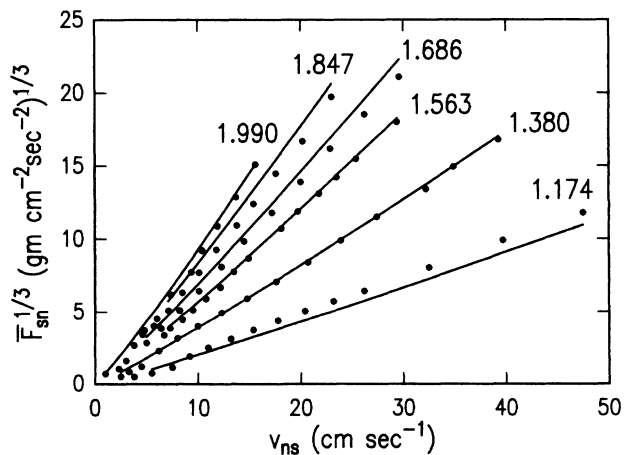


FIG. 25. Predicted mutual friction force as a function of temperature and driving velocity. The dots are the measurements of Brewer and Edwards (Ref. 26) in a 0.0366-cm-glass capillary.

viation of the data. The theory presented here, however, predicts that it is

$$(\kappa/4\pi) \ln(1/c_1 \bar{L}^{1/2} a_0) \bar{L}^{1/2},$$

not  $\bar{L}^{1/2}$ , that should be proportional to  $v_{ns}$ . When the data are plotted according to this prescription, perfect agreement is obtained. One concludes that even the weak logarithmic corrections predicted by the theory are clearly observed, and that the nonzero velocity intercept, ubiquitous in the extensive literature of the field, is an artifact of trying to fit the functional form of Eq. (12) by a straight line. This has also been noticed by Swanson and Donnelly.<sup>15</sup>

A more wide-ranging comparison between theory and experiment is shown in Fig. 27. The great majority of experiments on fully developed superfluid turbulence have measured  $\bar{F}_{sn}$ , which can be unambiguously determined from the temperature gradient. Equation (20) can be applied to such measurements to deduce  $c_L^2 \bar{I}_{\parallel} - c_L^3 \bar{I}_I$ . For the purpose of estimating  $\beta \simeq (\kappa/4\pi) \ln(1/c_1 \bar{L}^{1/2} a_0)$  in this equation,  $\bar{L}$  can be obtained with sufficient accuracy from Eq. (23), by assuming the homogeneity conditions  $\bar{I}_{\parallel} = \frac{2}{3}$ ,  $\bar{I}_I = 0$ , and  $c_1$  can be read off Fig. 22. The main source of uncertainty in this kind of data reduction comes in determining the relationship between temperature and  $\alpha$  appropriate to each particular experiment. We have simply used Fig. 24, which may account for some of the residual scatter in the figure. In addition,

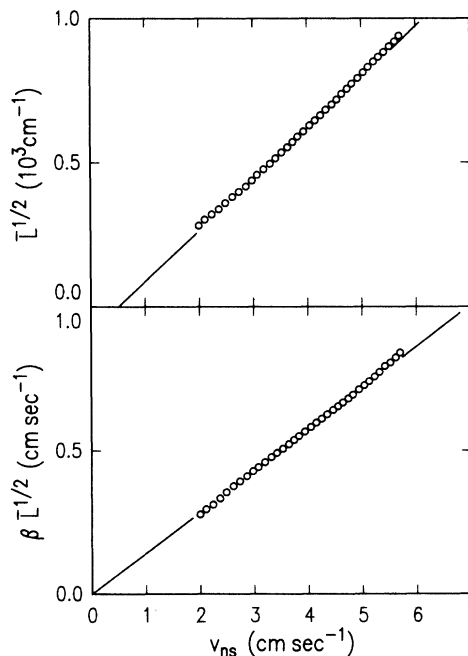


FIG. 26. Data of Martin and Tough (Ref. 27) exhibiting the logarithmic corrections predicted by our theory. The two ways of plotting the data are discussed in the text.

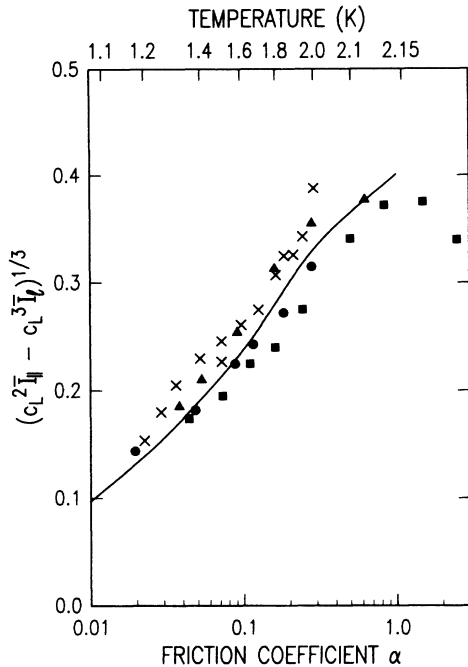


FIG. 27. Comparison of the theoretically predicted mutual friction force coefficient with selected experiments. Triangles are from Ref. 5, dots from Ref. 26, crosses from Ref. 28, and squares from Ref. 20. In all of these experiments,  $\alpha$  is varied by changing the temperature.

since historically every author has reduced his data in a different way, none of them strictly correct from our present perspective, a fair amount of tedious data reconstruction is required, contributing its own ambiguities. There have been numerous other measurements<sup>4</sup> of  $\bar{F}_{sn}$ . They could all be added to Fig. 27 without changing it

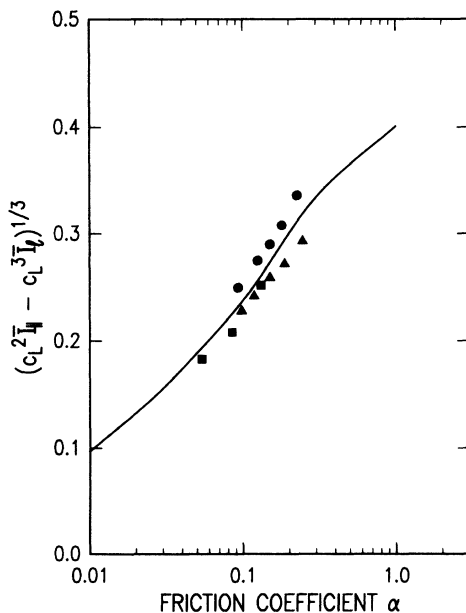


FIG. 28. Comparison of the theoretically predicted mutual friction force coefficient with experiments where  $\alpha$  is varied by changing the pressure. The dots are from Ref. 30, while the squares and triangles are from Ref. 29.

very much. However, the points plotted here already represent quite a variety of experimental conditions: pure superflow and counterflow, channel sizes ranging from 0.0366 to 1 cm, channel shapes varying from circular to rectangular with a 10:1 aspect ratio, and line-length densities covering a range of  $10^3$  to  $10^8$ . The properties of the fully turbulent state are manifestly independent of all such details and are seen to be in excellent absolute agreement with the predictions of the theory presented here.

It is possible in the laboratory to vary the friction constants by changing the pressure or the  $^3\text{He}$  impurity concentration, rather than the temperature. Measurements of this kind provide an independent check on the theory, and in particular test the notion that the properties of the vortex tangle are determined almost entirely by the value of  $\alpha$ . Figure 28, adapted from a very recent paper by Mimura and Luszczynski,<sup>29</sup> makes it obvious that equally good agreement between theory and experiment is obtained when  $\alpha$  is tuned by changing the pressure.

Finally, it is apparent from the numbers given in Table I that the internal structure of the vortex tangle depends

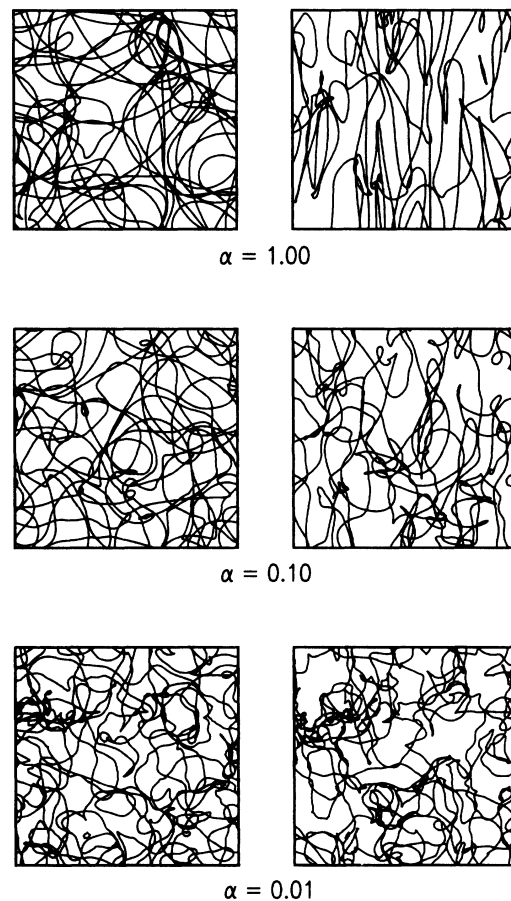


FIG. 29. Illustration of the predicted changes in the internal structure of the vortex tangle as  $\alpha$  is varied. Each figure on the left shows the computational volume at a particular instant, viewed along the flow direction. The corresponding figure on the right shows the same instant viewed across the flow direction. These tangles were generated using periodic boundary conditions with mixing, and the driving velocities were chosen to give  $\bar{L}$  approximately equal to 47 in each instance.

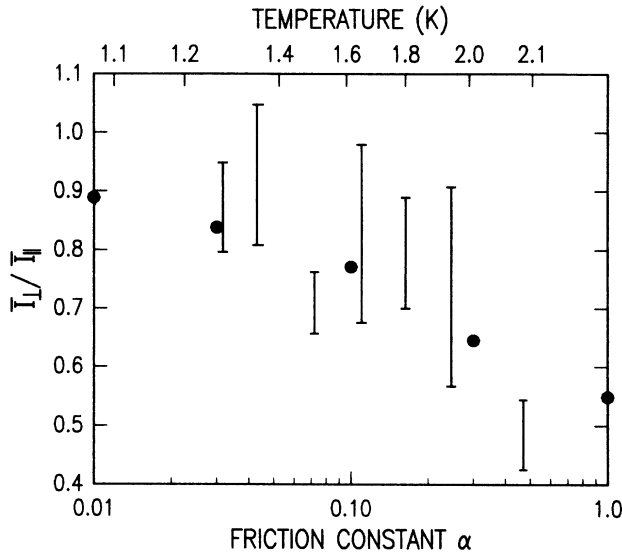


FIG. 30. Comparison of the computed anisotropy ratio (dots) with the experimental results of Ref. 21 (vertical bars).

on  $\alpha$ . For example, the tangle changes from being quite anisotropic at large  $\alpha$  to a more isotropic structure as the friction constant is decreased. Also, the variation in  $c_1$  and  $c_2$  shows that the vortex tangle becomes increasingly kinky as  $\alpha$  is made smaller. The sequence of snapshots given in Fig. 29 exhibits this evolution quite clearly. The variations seen here can be understood qualitatively as being due to the fact that the regions of high curvature, and the associated three-dimensionally random motion of the vortex line, tend to be increasingly damped out as  $\alpha$  becomes larger, whereas the two-dimensional frictional growth becomes relatively more dominant.

A recent set of experiments by Wang, Swanson, and Donnelly<sup>21</sup> provides a test of some of these more refined predictions of the theory. These authors have measured the spanwise and streamwise second-sound absorption coefficients  $\alpha_{\perp}$  and  $\alpha_{\parallel}$ . As discussed in connection with Eq. (26), their results can be analyzed<sup>31</sup> to yield  $\bar{I}_{\perp}\bar{L}$  and  $\bar{I}_{\parallel}\bar{L}$ . The ratio of these is just the anisotropy ratio  $\bar{I}_{\perp}/\bar{I}_{\parallel}$ , shown in Fig. 30. Use of the relation given in Eq. (18) also allows the extraction of  $\bar{L}$ . In addition, Wang *et al.* measure the mutual friction force directly from the temperature gradient, to obtain  $(\bar{I}_{\parallel} - c_L\bar{I}_{\perp})\bar{L}$  from Eq. (23).

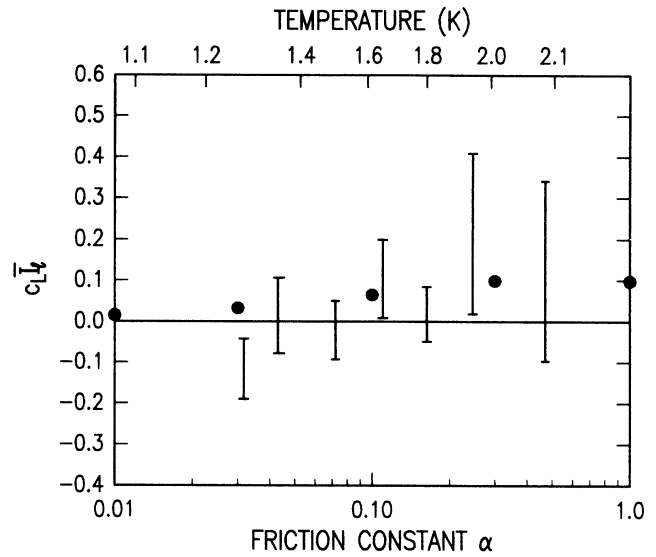


FIG. 31. Comparison of the predicted vortex drift factor (dots) with the data of Ref. 21 (vertical bars).

Thus they can derive the quantity  $c_L\bar{I}_{\perp}$  from their measurements. From Eq. (22) one can see that this quantity approximates  $\bar{v}_l/v_{ns}$ , and the authors make this identification. Figure 31 shows how their experimental estimates compare with theory.

The authors of Ref. 21 make it clear that the extraction of the anisotropy ratio and the line-drift velocity from their experiments is a difficult business. The error limits they quote, i.e., those shown in Figs. 30 and 31, are correspondingly conservative. Nevertheless, it is very encouraging to observe that their results, which represent an entirely new kind of experimental information about the superfluid turbulent state, once again turn out to be in good agreement with the predictions of our theory. Figure 30 especially indicates that the predicted structural variation illustrated in Fig. 29 does indeed occur.

#### ACKNOWLEDGMENTS

I wish to thank J. T. Tough for many helpful discussions and useful suggestions, and R. J. Donnelly for a number of stimulating conversations.

<sup>1</sup>R. P. Feynman, in *Progress in Low Temperature Physics*, edited by C. J. Gorter (North-Holland, Amsterdam, 1955), Vol. I, p. 15.

<sup>2</sup>H. E. Hall and W. F. Vinen, *Proc. R. Soc. London, Ser. A* **238**, 204 (1956); **238**, 215 (1956).

<sup>3</sup>G. W. Rayfield and F. Reif, *Phys. Rev.* **136**, A1194 (1964).

<sup>4</sup>For recent reviews see J. T. Tough, in *Progress in Low Temperature Physics*, edited by D. F. Brewer (North-Holland, Amsterdam, 1982), Vol. VIII, p. 133; and also R. J. Donnelly and

C. E. Swanson, *J. Fluid Mech.* **173**, 387 (1986).

<sup>5</sup>W. F. Vinen, *Proc. R. Soc. London, Ser. A* **240**, 114 (1957); **240**, 128 (1957); **242**, 493 (1957); **243**, 400 (1957).

<sup>6</sup>K. W. Schwarz, *Phys. Rev. B* **18**, 245 (1978).

<sup>7</sup>K. W. Schwarz, *Phys. Rev. Lett.* **49**, 283 (1982).

<sup>8</sup>K. W. Schwarz, *Phys. Rev. B* **31**, 5782 (1985).

<sup>9</sup>The notational distinction of Ref. 8 between the applied superfluid field  $v_{s,a}$  and  $v_n$  is here dropped,  $v_{s,a}$  being replaced by  $v_s$  and interpreted as a local average of the

- superfluid velocity field. The assumption is that random fluctuations in  $\mathbf{v}_s$  due to other nearby parts of the vortex tangle are either unimportant or average to zero over time scales short compared to other significant time scales.
- <sup>10</sup>The friction parameters are related to the conventional Hall-Vinen parameters  $B$  and  $B'$  by  $\alpha = \rho_n B / 2\rho$  and  $\alpha' = \rho_n B' / 2\rho$ . A table of  $\alpha, \alpha'$  versus temperature is given in Ref. 8.
- <sup>11</sup>W. T. Ashurst and D. I. Meiron, *Phys. Rev. Lett.* **58**, 1632 (1987); A. Pumir and R. M. Kerr, *ibid.*, **58**, 1636 (1987).
- <sup>12</sup>From the theoretical point of view,  $L$  depends on  $\alpha$  and  $\alpha'$ , which in turn are functions of  $T$  and  $P$ .
- <sup>13</sup>D. D. Awschalom, F. P. Milliken, and K. W. Schwarz, *Phys. Rev. Lett.* **53**, 1372 (1984).
- <sup>14</sup>See, however, Fig. 18 in Sec. III, which implies that some nonuniformity corrections may arise when  $L$  becomes small.
- <sup>15</sup>C. E. Swanson and R. J. Donnelly, *J. Low Temp. Phys.* **61**, 363 (1980).
- <sup>16</sup>Critical angles arise when considering the interaction of the vortex tangle with rough channel walls.
- <sup>17</sup>As it happens, the dependence of the vortex-tangle properties on  $\alpha$  and  $\alpha'$  turns out to be relatively weak. This is fortunate since, strictly speaking,  $\alpha$  and  $\alpha'$  are not constants in Eq. (3). Because of the complex interactions between the excitation gas and the vortex core,  $\alpha$  and  $\alpha'$  exhibit a residual dependence on the relative velocity between the normal fluid and the core. More generally, they can also depend on the history of this relative velocity, leading for example to a frequency dependence in oscillating flow. While such effects can affect the absolute values of the scaling coefficients, they are not large enough to significantly distort the scaling arguments. The subject has most recently been discussed by C. E. Swanson, W. T. Wagner, R. J. Donnelly, and C. F. Barenghi, *J. Low. Temp. Phys.* **66**, 263 (1987).
- <sup>18</sup>See, for example, K. W. Schwarz, *Phys. Rev. Lett.* **50**, 364 (1983); **57**, 1448 (1986).
- <sup>19</sup>D. D. Awschalom and K. W. Schwarz, *Phys. Rev. Lett.* **52**, 49 (1984).
- <sup>20</sup>C. E. Swanson, Ph.D. thesis, University of Oregon, 1985.
- <sup>21</sup>R. T. Wang, C. E. Swanson, and R. J. Donnelly, *Phys. Rev. B* **36**, 5240 (1987).
- <sup>22</sup>F. P. Milliken, K. W. Schwarz, and C. W. Smith, *Phys. Rev. Lett.* **48**, 1204 (1982).
- <sup>23</sup>It is interesting to note that if the real-wall results are averaged over the whole channel rather than just the center portion, the agreement with the values calculated using periodic boundary conditions is improved considerably. See Fig. 18.
- <sup>24</sup>The effects of the logarithmic correction to  $\Delta$  should not be confused with the issues raised by the logarithmic variation of  $\beta$ . As will be discussed in Sec. IV, the latter leads to small but quantifiable effects which are clearly observed experimentally. Of course, the assumption throughout is that  $|\overline{s''}| a_0 \ll 1$ .
- <sup>25</sup>The differences in the converged value of  $\overline{L}^{1/2}$  in Figs. 9, 13, and 14 arise from the fact that these calculations were carried out using somewhat different values of  $\Delta$ .
- <sup>26</sup>D. F. Brewer and D. O. Edwards, *Philos. Mag.* **7**, 721 (1962).
- <sup>27</sup>K. P. Martin and J. T. Tough, *Phys. Rev. B* **27**, 2788 (1983).
- <sup>28</sup>L. B. Opatowsky and J. T. Tough, *Phys. Rev. B* **24**, 5420 (1981).
- <sup>29</sup>K. Mimura and K. Luszczynski, Proceedings of the 18th International Conference on Low Temperature Physics, Kyoto, 1987 [*Jpn. J. Appl. Phys.* **26**, 93 (1987)].
- <sup>30</sup>D. F. Brewer and D. O. Edwards, *J. Low Temp. Phys.* **43**, 327 (1981).
- <sup>31</sup>The notation of Ref. 21 differs from ours.  $\overline{I}_\parallel \overline{L}$  and  $\overline{I}_\perp \overline{L}$  are called  $L_A$  and  $L_T$ , respectively.  $(\overline{I}_\parallel - c_L \overline{I}_\perp)$  is denoted by  $G$ .